Signal Processing: Image Communication 98 (2021) 116400

Contents lists available at ScienceDirect

Signal Processing: Image Communication

journal homepage: www.elsevier.com/locate/image

A unified framework for damaged image fusion and completion based on low-rank and sparse decomposition

Minghong Xie[a], Jiaxin Wang[a], Yafei Zhang[a,b,*]

[a] *Faculty of Information Engineering and Automation, Kunming University of Science and Technology, Kunming 650500, China*
[b] *Key Laboratory of Artificial Intelligence in Yunnan Province, Kunming University of Science and Technology, Kunming 650500, China*

ARTICLE INFO

Keywords:
Image fusion
Image completion
Image decomposition
Low-rank and sparse representation
Dictionary learning

ABSTRACT

Image fusion can integrate the complementary information of multiple images. However, when the images to be fused are damaged, the existing fusion methods cannot recover the lost information. Matrix completion, on the other hand, can be used to recover the missing information of the image. Therefore, the step-by-step operation of image fusion and completion can fuse the damaged images, but it will cause artifact propagation. In view of this, we develop a unified framework for image fusion and completion. Within this framework, we first assume that the image is superimposed by low-rank and sparse components. To obtain the separation of different components to fuse and restore them separately, we propose a low-rank and sparse dictionary learning model. Specifically, we impose low-rank and sparse constraints on low-rank dictionary and sparse component respectively to improve the discrimination of learned dictionaries and introduce the condition constraints of low-rank and sparse components to promote the separation of different components. Furthermore, we integrate the low-rank characteristic of the image into the decomposition model. Based on this design, the lost information can be recovered with the decomposition of the image without using any additional algorithm. Finally, the maximum l_1-norm fusion scheme is adopted to merge the coding coefficients of different components. The proposed method can achieve image fusion and completion simultaneously in the unified framework. Experimental results show that this method can well preserve the brightness and details of images, and is superior to the compared methods according to the performance evaluation.

1. Introduction

Image fusion, by synthesizing the complementary information of multiple images of the same scene through a specific algorithm, can generate a new image that describes the scene information more accurately. In order to improve the fusion quality, a large number of image fusion methods have been proposed, which can be generally divided into two categories, namely spatial domain methods and transform domain methods. The spatial domain-based methods measure the definition of image blocks or regions directly in the pixel space and compare their clarity to fuse the images [1–4]. However, the block-based methods have a block effect. For the region-based methods, the quality of fused images can be severely affected by the accuracy of image segmentation, which itself is a challenging task [1]. In recent years, the transform domain-based methods have attracted more attention, which consist of three steps: image transform, transform coefficient fusion, and inverse transform. The common transform domain-based fusion methods include Discrete Wavelet Transform (DWT)-based methods [5,6], Curvelet Transform (CVT)-based methods [7], Non-Subsampled Contourlet Transform (NSCT)-based methods [8–10] and Sparse Representation (SR)-based methods [11–19], etc.

The existing image fusion methods mainly focus on the fusion of lossless images, while the research on damaged image fusion is scarce. However, in the process of image acquisition or transmission, the acquired image will lose information if the imaging device or transmission channel fails. Due to the missing pixels in the images to be fused, the fusion effects of the existing fusion methods are very poor, thus limiting the further application of fusion results. Therefore, it is practical to conduct research on damaged image fusion. The restoration of damaged images can be regarded as the problem of matrix completion, where all elements including the missing ones of the matrix can be recovered according to its low-rank characteristic. A feasible solution for realizing damaged image fusion are to perform image fusion and completion separately. Namely, the damaged images to be fused are recovered first and then fused, or are fused first, and then the fusion result is recovered. However, this kind of step-by-step operation will inevitably

---

[*] Correspondence to: School of Information Engineering and Automation, Kunming University of Science and Technology, 727 Jingming South Road, Chenggong District, Kunming 650500, China.
E-mail address: zyfeimail@163.com (Y. Zhang).

https://doi.org/10.1016/j.image.2021.116400
Received 18 November 2020; Received in revised form 12 June 2021; Accepted 21 July 2021

propagate artifacts generated in the first step to the next step, thereby reducing the visual perception quality of the final results. Consequently, it is necessary to perform image fusion and completion simultaneously.

It is found that the image content has a strong correlation, so it shows low-rank morphological characteristics. Inspired by this phenomenon and the idea of cartoon texture decomposition [20], we build a unified framework of image fusion and completion based on the low-rank and sparse representation theory. It can perform image fusion and completion simultaneously. The schematic diagram of the proposed framework is illustrated in Fig. 1. We can see that the method proposed in this paper mainly includes three parts, namely, discriminative dictionary learning (DDL), image decomposition and completion (IDC), and fusion of the coding coefficients of different components. In DDL, we propose a low-rank and sparse dictionary joint learning model based on the theory of cartoon texture decomposition. In IDC, we develop an image decomposition model to separate the low-rank and sparse components. In this processing, the missing pixels are completed with the separation of low-rank and sparse components. The low-rank and sparse coefficients are fused respectively based on the maximum l_1-norm fusion rule.

The main contributions are summarized as follows:

1. To achieve the fusion of damaged images, we establish a unified image fusion and completion framework, which can perform image fusion and completion simultaneously. The proposed method can also avoid artifact propagation which will be caused by the step-by-step operation of image fusion and completion.
2. We formulate a novel low-rank and sparse dictionary learning model for image decomposition. To improve the discrimination ability of learned dictionaries, the low-rank constraint $\|\boldsymbol{D}_l\|_*$ and sparse constraint $\|\boldsymbol{D}_s\boldsymbol{Z}_s\|_1$ are imposed on low-rank dictionary and sparse component, respectively. Moreover, in order to reduce the information loss caused by image decomposition, we propose to make the sum of the low-rank component $\boldsymbol{Y}_l$ and sparse component $\boldsymbol{Y}_s$ as equal as possible to the original image $\boldsymbol{Y}$.
3. We develop an image decomposition and completion model, in which the damaged images can be decomposed into low-rank and sparse components, and the lost information can be effectively recovered during the separation of different components. Extensive experimental results show the proposed method can better preserve the brightness and details of the original images and outperforms the alternative methods in terms of visual quality and performance evaluation.

The remainder of this paper is organized as follows. Section 2 briefly introduces related work of image fusion based on matrix completion and multi-component analysis. Section 3 presents the models of low-rank sparse dictionary learning, image decomposition and completion. The optimization algorithms of the proposed models are described in Section 4. Then, the image fusion scheme is introduced in Section 5. Section 6 reports the experimental results with discussions.

2. Related work

2.1. Matrix completion

In the process of image acquisition and transmission, some pixels will be lost due to the faults of the imaging equipment or transmission channel. Matrix completion aims to recover a complete matrix from a matrix with missing elements. Therefore, the restoration of missing pixels can be considered as the matrix completion problem. Assuming that $\boldsymbol{X} \in \mathbb{R}^{m\times n}$ is the underlying complete matrix of the incomplete data matrix $\boldsymbol{M} \in \mathbb{R}^{m\times n}$, the matrix completion problem can be formulated as:

$$\min_{\boldsymbol{X}} \|\boldsymbol{X}\|_* \qquad s.t. \qquad \boldsymbol{P}_\Omega(\boldsymbol{X}) = \boldsymbol{P}_\Omega(\boldsymbol{M}) \tag{1}$$

where $\|\cdot\|_*$ is the nuclear norm, $\boldsymbol{P}_\Omega$ is the orthogonal projection operator that keeps the entries in Ω unchanged and sets those on the outside to zero [21], and Ω is the set of indices of the known samples in $\boldsymbol{M}$. If $(i,j)\in\Omega$, $\boldsymbol{P}_\Omega(\boldsymbol{M}) = \boldsymbol{M}_{ij}$, else, $\boldsymbol{P}_\Omega(\boldsymbol{M}) = 0$.

Matrix completion problem can be solved by nuclear norm minimization, which often involves singular value thresholding. Cai et al. [22] proposed the Singular Value Thresholding (SVT) algorithm to solve the matrix completion problem. This algorithm could obtain the optimal solution with a low-rank structure, but its convergence speed was slow. In the work of Toh et al. [23], the Accelerated Proximal Gradient (APG) algorithm was proposed, which incorporated a linear search acceleration algorithm in the iterative process. Compared with the above two methods, the Inexact Augmented Lagrange Multipliers (IALM) algorithm constructed by Lin et al. [24] showed faster convergence speed and higher accuracy. Zhang et al. [25] proposed the truncated nuclear norm regularization model, which only retained the larger singular value whereas the smaller singular value was discarded. With these practical and efficient algorithms, matrix completion has been successfully applied to different fields, such as image inpainting and recommendation system.

2.2. Multi-component analysis based image fusion

The multi-component analysis based image fusion methods are to decompose the image into uncorrelated components, and then fuse each component separately. In 2014, Jiang et al. [26] first proposed the morphological component analysis based fusion method, which decomposed the image into cartoon and texture components. The image decomposition model was expressed as:

$$\left\{\boldsymbol{\alpha}_C, \boldsymbol{\alpha}_T\right\} = \arg\min_{\boldsymbol{\alpha}_C,\boldsymbol{\alpha}_T} \left\{\|\boldsymbol{\alpha}_C\|_1 + \|\boldsymbol{\alpha}_T\|_1\right\} \quad s.t. \quad \boldsymbol{X} = \boldsymbol{\phi}_C\boldsymbol{\alpha}_C + \boldsymbol{\phi}_T\boldsymbol{\alpha}_T \tag{2}$$

where $\boldsymbol{X} \in \mathbb{R}^{m\times n}$ was the source image, $\boldsymbol{\phi}_C$ and $\boldsymbol{\phi}_T$ represented cartoon dictionary and texture dictionary respectively, $\boldsymbol{\alpha}_C$ and $\boldsymbol{\alpha}_T$ were the sparse coding coefficients of cartoon and texture components respectively.

After obtaining $\boldsymbol{\alpha}_C$ and $\boldsymbol{\alpha}_T$, the sparse coding coefficients of cartoon and texture components were fused respectively. Then the fused coefficients of each component were multiplied by the corresponding dictionary to get the fused cartoon and texture components. Finally, the final fusion result was obtained by superposition of these two components. As mentioned above, how to build a dictionary model to obtain a corresponding dictionary of different components and how to build an image decomposition model to decompose the image into different components are two key issues in multi-component analysis-based image fusion. Based on these two problems, a large number of image fusion algorithms based on multi-component analysis have emerged.

For instance, Liu et al. [27] proposed a multi-focus image fusion method based on image decomposition. In this method, an improved iterative weighted decomposition algorithm was used to decompose the multi-focus source image into cartoon component and texture component. The analytical dictionaries of the curvelet and local Discrete Cosine Transform (DCT) were adopted. The Vese–Osher (VO) model was implemented for image decomposition, and sub-dictionaries were trained to enhance the sparse representation ability by Zhu et al. [15]. Zhang et al. [28] proposed an image fusion method based on the analysis–synthesis dictionary, in which the complementary representation mechanism of analysis and synthesis sparse representation was integrated into the dictionary learning and image decomposition model. The above fusion algorithms based on multi-component analysis can achieve good fusion results for clear images. On the other hand, for the fusion of images with noise, Li et al. proposed two different methods [12,29]. A medical image fusion, denoising, and enhancement method based on low-rank sparse decomposition was proposed in the work of Li et al. [12]. In the image decomposition model, weighted nuclear norm and sparse constraint were applied to sparse components to

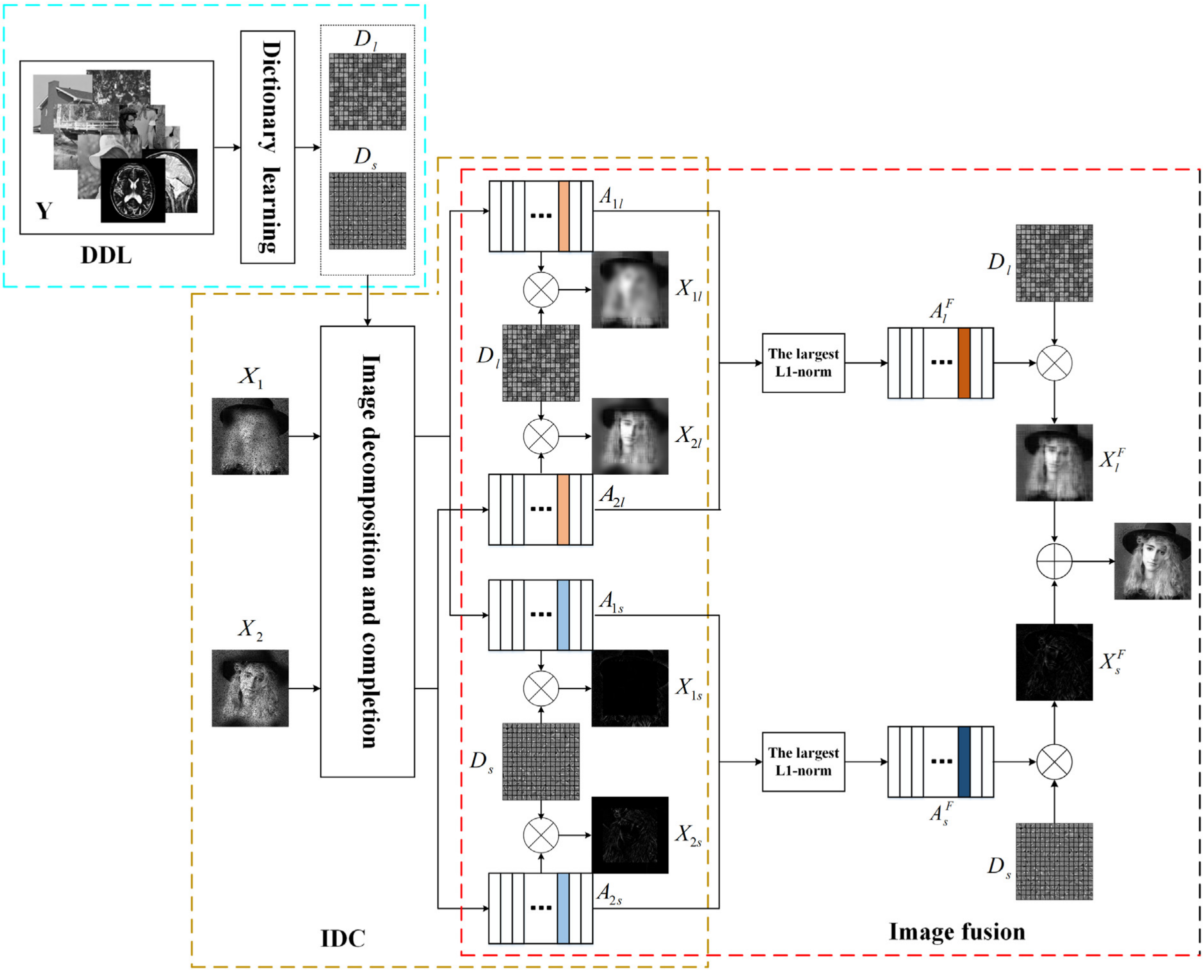

Fig. 1. The schematic diagram of the proposed algorithm.

remove noise and retain texture details. The low-rank sparse regularization was added to improve the discrimination ability of the dictionary in the dictionary learning model. Li et al. [29] decomposed the image into coarse-scale and fine-scale components and then designed the corresponding dictionary learning model.

Nonetheless, the relevant research is scarce for the fusion of damaged images. One feasible solution is the step-by-step operation of image fusion and completion, which will propagate the artifacts between two steps. Therefore, based on image multi-component analysis and matrix completion, we develop a unified framework of image fusion and completion for damaged image fusion and establish the corresponding dictionary learning and image decomposition models.

3. Proposed method

3.1. Low-rank and sparse dictionary learning

In this section, we develop a novel low-rank and sparse dictionary learning model for image decomposition. Let $\boldsymbol{Y}$ denote the entire training set that consists of N image patches, that is, $Y = [\boldsymbol{y}_1, \boldsymbol{y}_2, \ldots, \boldsymbol{y}_N]$. $\boldsymbol{y}_i \in \mathbb{R}^W$ is a column vector version of an image patch of size $\sqrt{W} \times \sqrt{W}$. The low-rank and sparse dictionaries can be learned by solving:

$$\left\{ \begin{array}{l} \boldsymbol{D}_l, \boldsymbol{D}_s \\ \boldsymbol{Z}_l, \boldsymbol{Z}_s \end{array} \right\} = \arg \min_{\boldsymbol{D}_l, \boldsymbol{D}_s, \boldsymbol{Z}_l, \boldsymbol{Z}_s} \left\{ \|\boldsymbol{Y} - \boldsymbol{D}_l \boldsymbol{Z}_l - \boldsymbol{D}_s \boldsymbol{Z}_s\|_F^2 + \lambda_1 \|\boldsymbol{Z}_l\|_{2,1} + \lambda_2 \|\boldsymbol{Z}_s\|_1 \right\} \tag{3}$$

where $\boldsymbol{D}_l \in \mathbb{R}^{W \times K}$ and $\boldsymbol{D}_s \in \mathbb{R}^{W \times K}$ denote the low-rank and sparse dictionaries respectively; $\boldsymbol{Z}_l \in \mathbb{R}^{K \times N}$ and $\boldsymbol{Z}_s \in \mathbb{R}^{K \times N}$ denote the coding coefficients of low-rank and sparse components over dictionaries $\boldsymbol{D}_l$ and $\boldsymbol{D}_s$; λ_1 and λ_2 are the balance parameters.

In Eq. (3), the regularization terms $\|\boldsymbol{Z}_l\|_{2,1}$ and $\|\boldsymbol{Z}_s\|_1$ are used to force information with similar or identical characteristics to be represented by the same atom in the dictionary, that is, to make the coding coefficients of low-rank and sparse components sparse. In low-rank and sparse decomposition, the performance of the dictionary is very important. In order to improve the discrimination of dictionaries $\boldsymbol{D}_l$ and $\boldsymbol{D}_s$, the model described by Eq. (3) can be modified as:

$$\left\{ \begin{array}{l} \boldsymbol{D}_l, \boldsymbol{D}_s \\ \boldsymbol{Z}_l, \boldsymbol{Z}_s \end{array} \right\} = \arg \min_{\boldsymbol{D}_l, \boldsymbol{D}_s, \boldsymbol{Z}_l, \boldsymbol{Z}_s} \left\{ \|\boldsymbol{Y} - \boldsymbol{D}_l \boldsymbol{Z}_l - \boldsymbol{D}_s \boldsymbol{Z}_s\|_F^2 + \lambda_1 \|\boldsymbol{Z}_l\|_{2,1} \right. \\ \left. + \lambda_2 \|\boldsymbol{Z}_s\|_1 + \lambda_3 \|\boldsymbol{D}_l\|_* + \lambda_4 \|\boldsymbol{D}_s \boldsymbol{Z}_s\|_1 \right\} \tag{4}$$

where λ_3 and λ_4 are the balance parameters.

In Eq. (4), $\boldsymbol{D}_l$ is utilized to represent low-rank components of the input image, so it should also be low-rank. Therefore, we introduce regularization term $\|\boldsymbol{D}_l\|_*$ to refine the solution space of $\boldsymbol{D}_l$. Moreover, since the sparse components are linearly related to the atoms of dictionary $\boldsymbol{D}_s$ and they have the same morphological properties, thus $\|\boldsymbol{D}_s \boldsymbol{Z}_s\|_1$ can also be utilized to regularize the solution space of $\boldsymbol{D}_s$.

In addition, to further improve the accuracy of the dictionary, we introduce the constraint condition $\boldsymbol{Y}_l = \boldsymbol{D}_l \boldsymbol{Z}_l$ and $\boldsymbol{Y}_s = \boldsymbol{D}_s \boldsymbol{Z}_s$. Then

Eq. (4) can be rewritten as:

$$\begin{Bmatrix} \boldsymbol{D}_l, \boldsymbol{D}_s \\ \boldsymbol{Z}_l, \boldsymbol{Z}_s \\ \boldsymbol{Y}_l, \boldsymbol{Y}_s \end{Bmatrix} = \arg \min_{\boldsymbol{D}_l,\boldsymbol{D}_s,\boldsymbol{Z}_l,\boldsymbol{Z}_s,\boldsymbol{Y}_l,\boldsymbol{Y}_s} \{ \|\boldsymbol{Y} - \boldsymbol{Y}_l - \boldsymbol{Y}_s\|_F^2 + \lambda_1 \|\boldsymbol{Z}_l\|_{2,1} + \lambda_2 \|\boldsymbol{Z}_s\|_1 + \lambda_3 \|\boldsymbol{D}_l\|_* + \lambda_4 \|\boldsymbol{Y} - \boldsymbol{Y}_l\|_1 \} \quad s.t. \quad \boldsymbol{Y}_l = \boldsymbol{D}_l \boldsymbol{Z}_l, \quad \boldsymbol{Y}_s = \boldsymbol{D}_s \boldsymbol{Z}_s \tag{5}$$

3.2. Image decomposition and image completion

Let $\boldsymbol{X}$ denote the underlying complete image of incomplete observed image $\boldsymbol{M}$. Assuming that the observation image $\boldsymbol{M}$ is divided into P patches with the size of $\sqrt{W} \times \sqrt{W}$, and each image patch is reshaped into a column vector, then $\boldsymbol{M}$ can be expressed as $\boldsymbol{M} = [\boldsymbol{m}_1, \boldsymbol{m}_2, \dots, \boldsymbol{m}_P] \in \mathbb{R}^{W \times P}$, in which $\boldsymbol{m}_i \in \mathbb{R}^W$ is a column vector rearranged by the ith image patch. According to the matrix completion model in Eq. (1) and the learned dictionaries $\boldsymbol{D}_l$ and $\boldsymbol{D}_s$, the developed image decomposition and completion model can be formulated as:

$$\{\boldsymbol{A}_l, \boldsymbol{A}_s, \boldsymbol{X}\} = \arg \min_{\boldsymbol{A}_l,\boldsymbol{A}_s,\boldsymbol{X}} \{ \|\boldsymbol{X} - \boldsymbol{D}_l \boldsymbol{A}_l - \boldsymbol{D}_s \boldsymbol{A}_s\|_F^2 + \tau \|\boldsymbol{X}\|_* + \beta_1 \|\boldsymbol{D}_l \boldsymbol{A}_l\|_* + \beta_2 \|\boldsymbol{D}_s \boldsymbol{A}_s\|_1 + \beta_3 \|\boldsymbol{A}_l\|_{2,1} + \beta_4 \|\boldsymbol{A}_s\|_1 \} \quad s.t. \quad \boldsymbol{P}_\Omega(\boldsymbol{X}) = \boldsymbol{P}_\Omega(\boldsymbol{M}) \tag{6}$$

where τ and $\beta_i (i = 1, 2, \dots, 4)$ are the regularization parameters. $\boldsymbol{X} = [\boldsymbol{x}_1, \boldsymbol{x}_2, \dots, \boldsymbol{x}_P] \in \mathbb{R}^{W \times P}$, $\boldsymbol{x}_i (i = 1, 2, \dots, P)$ denotes the ith patch of underlying complete image. $\boldsymbol{A}_l = [\boldsymbol{a}_{l,1}, \boldsymbol{a}_{l,2}, \dots, \boldsymbol{a}_{l,P}] \in \mathbb{R}^{K \times P}$ and $\boldsymbol{A}_s = [\boldsymbol{a}_{s,1}, \boldsymbol{a}_{s,2}, \dots, \boldsymbol{a}_{s,P}] \in \mathbb{R}^{K \times P}$ are the coding coefficients of low-rank and sparse components of the complete image $\boldsymbol{X}$, respectively.

Since the functions in Eqs. (5) and (6) are convex, they can be solved by alternative iterative method.

4. Optimization and algorithm

4.1. Optimization of dictionary learning model

Eq. (5) describes a constrained optimization problem, and it can be solved effectively by inexact Augmented Lagrangian multiplier method [24]. The augmented Lagrangian function can be expressed by:

$$\begin{Bmatrix} \boldsymbol{D}_l, \boldsymbol{D}_s \\ \boldsymbol{Z}_l, \boldsymbol{Z}_s \\ \boldsymbol{Y}_l, \boldsymbol{Y}_s \end{Bmatrix} = \arg \min_{\boldsymbol{D}_l,\boldsymbol{D}_s,\boldsymbol{Z}_l,\boldsymbol{Z}_s,\boldsymbol{Y}_l,\boldsymbol{Y}_s} \{ \|\boldsymbol{Y} - \boldsymbol{Y}_l - \boldsymbol{Y}_s\|_F^2 + \lambda_1 \|\boldsymbol{Z}_l\|_{2,1} + \lambda_2 \|\boldsymbol{Z}_s\|_1 + \lambda_3 \|\boldsymbol{D}_l\|_* + \lambda_4 \|\boldsymbol{Y} - \boldsymbol{Y}_l\|_1 + tr[\boldsymbol{U}_1^T(\boldsymbol{Y}_l - \boldsymbol{D}_l \boldsymbol{Z}_l)] + \frac{\mu_1}{2} \|\boldsymbol{Y}_l - \boldsymbol{D}_l \boldsymbol{Z}_l\|_F^2 + tr[\boldsymbol{U}_2^T(\boldsymbol{Y}_s - \boldsymbol{D}_s \boldsymbol{Z}_s)] + \frac{\mu_2}{2} \|\boldsymbol{Y}_s - \boldsymbol{D}_s \boldsymbol{Z}_s\|_F^2 \} \tag{7}$$

where $\boldsymbol{U}_1$ and $\boldsymbol{U}_2$ are the Lagrange multiplier, μ_1 and μ_2 $(\mu_1, \mu_2 > 0)$ are balance parameters, T denotes the transpose operation, and tr is an operator of finding the trace of a matrix.

4.1.1. Updating of $\mathbf{Y}_l$ *and* $\mathbf{Y}_s$

We update $\boldsymbol{Y}_l$ with $\boldsymbol{D}_l$, $\boldsymbol{D}_s$, $\boldsymbol{Z}_l$, $\boldsymbol{Z}_s$ and $\boldsymbol{Y}_s$ fixed. Thus, the objective function in Eq. (7) is reduced to:

$$\boldsymbol{Y}_l = \arg \min_{\boldsymbol{Y}_l} \{ \|\boldsymbol{Y} - \boldsymbol{Y}_l - \boldsymbol{Y}_s\|_F^2 + \lambda_4 \|\boldsymbol{Y} - \boldsymbol{Y}_l\|_1 + \frac{\mu_1}{2} \|\boldsymbol{Y}_l - \boldsymbol{D}_l \boldsymbol{Z}_l + \frac{\boldsymbol{U}_1}{\mu_1}\|_F^2 \} \tag{8}$$

The auxiliary variable $\widetilde{\boldsymbol{Y}_s}$ is introduced to solve Eq. (8) and it can be rewritten as:

$$\{\boldsymbol{Y}_l, \widetilde{\boldsymbol{Y}_s}\} = \arg \min_{\boldsymbol{Y}_l, \widetilde{\boldsymbol{Y}_s}} \{ \|\widetilde{\boldsymbol{Y}_s} - \boldsymbol{Y}_s\|_F^2 + \lambda_4 \|\widetilde{\boldsymbol{Y}_s}\|_1 + \|\widetilde{\boldsymbol{Y}_s} - (\boldsymbol{Y} - \boldsymbol{Y}_l)\|_F^2 + \frac{\mu_1}{2} \|\boldsymbol{Y}_l - \boldsymbol{D}_l \boldsymbol{Z}_l + \frac{\boldsymbol{U}_1}{\mu_1}\|_F^2 \} \tag{9}$$

where $\widetilde{\boldsymbol{Y}_s}$ can be updated by:

$$\widetilde{\boldsymbol{Y}_s} = \arg \min_{\widetilde{\boldsymbol{Y}_s}} \{ \|\widehat{\boldsymbol{Y}_s} - \widehat{\boldsymbol{I}} \widetilde{\boldsymbol{Y}_s}\|_F^2 + \lambda_4 \|\widetilde{\boldsymbol{Y}_s}\|_1 \} \tag{10}$$

where $\widehat{\boldsymbol{Y}_s} = [\boldsymbol{Y}_s; \boldsymbol{Y} - \boldsymbol{Y}_l]$, $\widehat{\boldsymbol{I}} = [\boldsymbol{I}_W; \boldsymbol{I}_W]$, $\boldsymbol{I}_W$ is the $W \times W$ identity matrix.

The above objective function is a typical l_1-norm minimization problem, which can be solved by the Two-Step Iterative Shrinkage/Thresholding (TwIST) algorithm [30] or Fast Iterative Shrinkage-Thresholding (FIST) algorithm [31]. Then, $\boldsymbol{Y}_l$ can be updated by:

$$\boldsymbol{Y}_l = \arg \min_{\boldsymbol{Y}_l} \{ \|\widetilde{\boldsymbol{Y}_s} - (\boldsymbol{Y} - \boldsymbol{Y}_l)\|_F^2 + \frac{\mu_1}{2} \|\boldsymbol{Y}_l - \boldsymbol{D}_l \boldsymbol{Z}_l + \frac{\boldsymbol{U}_1}{\mu_1}\|_F^2 \} \tag{11}$$

All terms in Eq. (11) are Frobenius norms, so it has analytic solutions:

$$\boldsymbol{Y}_l = \frac{1}{2 + \mu_1} (\mu_1 \boldsymbol{D}_l \boldsymbol{Z}_l - 2\widetilde{\boldsymbol{Y}_s} + 2\boldsymbol{Y} - \boldsymbol{U}_1) \tag{12}$$

Similarly, by fixing $\boldsymbol{D}_l$, $\boldsymbol{D}_s$, $\boldsymbol{Z}_l$, $\boldsymbol{Z}_s$ and $\boldsymbol{Y}_l$, $\boldsymbol{Y}_s$ can be updated:

$$\boldsymbol{Y}_s = \arg \min_{\boldsymbol{Y}_s} \{ \|\boldsymbol{Y} - \boldsymbol{Y}_l - \boldsymbol{Y}_s\|_F^2 + \frac{\mu_2}{2} \|\boldsymbol{Y}_s - \boldsymbol{D}_s \boldsymbol{Z}_s + \frac{\boldsymbol{U}_2}{\mu_2}\|_F^2 \} \tag{13}$$

which has a closed-form solution:

$$\boldsymbol{Y}_s = \frac{1}{2 + \mu_2} (\mu_2 \boldsymbol{D}_s \boldsymbol{Z}_s - 2\boldsymbol{Y}_l + 2\boldsymbol{Y} - \boldsymbol{U}_2) \tag{14}$$

4.1.2. Updating of $\mathbf{Z}_l$ *and* $\mathbf{Z}_s$

We optimize $\boldsymbol{Z}_l$ by fixing all other variables, and Eq. (7) can be re-formulated as:

$$\boldsymbol{Z}_l = \arg \min_{\boldsymbol{Z}_l} \{ \lambda_1 \|\boldsymbol{Z}_l\|_{2,1} + \frac{\mu_1}{2} \|\boldsymbol{Y}_l + \frac{\boldsymbol{U}_1}{\mu_1} - \boldsymbol{D}_l \boldsymbol{Z}_l\|_F^2 \} \tag{15}$$

The above objective function is a $l_{2,1}$-norm solution problem, which can be solved by the algorithm proposed in literature [32]. Similarly, we can update $\boldsymbol{Z}_s$ by:

$$\boldsymbol{Z}_s = \arg \min_{\boldsymbol{Z}_s} \{ \lambda_2 \|\boldsymbol{Z}_s\|_1 + \frac{\mu_2}{2} \|\boldsymbol{Y}_s + \frac{\boldsymbol{U}_2}{\mu_2} - \boldsymbol{D}_s \boldsymbol{Z}_s\|_F^2 \} \tag{16}$$

The l_1 minimization problem can be solved by either the TwIST or FIST algorithm.

4.1.3. Updating of $\mathbf{D}_l$ *and* $\mathbf{D}_s$

The low-rank dictionary $\boldsymbol{D}_l$ can be updated by fixing other parameters in Eq. (7):

$$\boldsymbol{D}_l = \arg \min_{\boldsymbol{D}_l} \{ \lambda_3 \|\boldsymbol{D}_l\|_* + \frac{\mu_1}{2} \|\boldsymbol{Y}_l + \frac{\boldsymbol{U}_1}{\mu_1} - \boldsymbol{D}_l \boldsymbol{Z}_l\|_F^2 \} \tag{17}$$

To solve $\boldsymbol{D}_l$, we introduce a relaxation variable $\boldsymbol{B}_l$:

$$\{\boldsymbol{D}_l, \boldsymbol{B}_l\} = \arg \min_{\boldsymbol{D}_l, \boldsymbol{B}_l} \{ \lambda_3 \|\boldsymbol{B}_l\|_* + \|\boldsymbol{D}_l - \boldsymbol{B}_l\|_F^2 + \frac{\mu_1}{2} \|\boldsymbol{Y}_l + \frac{\boldsymbol{U}_1}{\mu_1} - \boldsymbol{D}_l \boldsymbol{Z}_l\|_F^2 \} \tag{18}$$

$\boldsymbol{B}_l$ and $\boldsymbol{D}_l$ can be updated alternatively. The optimal solution of $\boldsymbol{B}_l$ can be obtained by solving the following optimization problem:

$$\boldsymbol{B}_l = \arg \min_{\boldsymbol{B}_l} \{ \|\boldsymbol{D}_l - \boldsymbol{B}_l\|_F^2 + \lambda_3 \|\boldsymbol{B}_l\|_* \} \tag{19}$$

This is a nuclear norm minimization problem and $\boldsymbol{B}_l$ can be solved by using the Singular Value Thresholding (SVT) algorithm [22]. After $\boldsymbol{B}_l$ is updated, $\boldsymbol{D}_l$ can be solved by:

$$\boldsymbol{D}_l = \arg \min_{\boldsymbol{D}_l} \{ \|\boldsymbol{B}_l - \boldsymbol{D}_l\|_F^2 + \frac{\mu_1}{2} \|\boldsymbol{Y}_l + \frac{\boldsymbol{U}_1}{\mu_1} - \boldsymbol{D}_l \boldsymbol{Z}_l\|_F^2 \} \tag{20}$$

which has closed-form solution:

$$\boldsymbol{D}_l = (2\boldsymbol{B}_l + \mu_1 \boldsymbol{Y}_l \boldsymbol{Z}_l^T + \boldsymbol{U}_1 \boldsymbol{Z}_l^T)(2\boldsymbol{I} + \mu_1 \boldsymbol{Z}_l \boldsymbol{Z}_l^T)^{-1} \tag{21}$$

Then, we optimize the sparse dictionary $\boldsymbol{D}_s$ by fixing $\boldsymbol{Y}_l$, $\boldsymbol{Y}_s$, $\boldsymbol{Z}_l$, $\boldsymbol{Z}_s$ and $\boldsymbol{D}_l$. Eq. (7) can be thus simplified as:

$$\boldsymbol{D}_s = \arg \min_{\boldsymbol{D}_s} \{ \|\boldsymbol{Y}_s + \frac{\boldsymbol{U}_2}{\mu_2} - \boldsymbol{D}_s \boldsymbol{Z}_s\|_F^2 \} \tag{22}$$

$\boldsymbol{D}_s$ has an analytic solution:

$$\boldsymbol{D}_s = (\boldsymbol{Y}_s \boldsymbol{Z}_s^T + \frac{\boldsymbol{U}_2}{\mu_2} \boldsymbol{Z}_s^T)(\boldsymbol{Z}_s \boldsymbol{Z}_s^T)^{-1} \tag{23}$$

The algorithm for learning low-rank and sparse dictionaries is summarized in Algorithm 1.

Algorithm 1 Algorithm for low-rank and sparse dictionaries learning

```
Input: $D_l$, $D_s$, $\lambda_i (i = 1, 2, \ldots, 4)$, maximum number of iterations $\mathcal{K}$.
Initialize: $Y_l$, $Y_s$, $Z_l$, $Z_s$, $U_1 = U_2 = 0$, $\mu_1 = \mu_2 = 0$, $max\mu_1 = max\mu_2 = 10^{30}$, $\rho = 1.1$
while $\mathcal{K}$ not be reached do
  1. Update the low-rank and sparse components $Y_l$ and $Y_s$
      (1) Update auxiliary variable $\widetilde{Y}_s$ by solving Eq. (10).
      (2) Update $Y_l$ by solving Eq. (12).
      (3) Update $Y_s$ by solving Eq. (14).
  2. Update the coding coefficients $Z_l$ and $Z_s$
      (1) Update $Z_l$ by solving Eq. (15).
      (2) Update $Z_s$ by solving Eq. (16).
  3. Update the dictionaries $D_l$ and $D_s$
      (1) Update auxiliary variable $B_l$ by solving Eq. (19).
      (2) Update $D_l$ by solving Eq. (21).
      (3) Update $D_s$ by solving Eq. (23).
  4. Update $U_1$, $U_2$, $\mu_1$ and $\mu_2$
      (1) $U_1 = U_1 + \mu_1 (Y_l - D_l Z_l)$.
      (2) $U_2 = U_2 + \mu_2 (Y_s - D_s Z_s)$.
      (3) $\mu_1 = \min(\rho\mu_1, \max \mu_1)$.
      (4) $\mu_2 = \min(\rho\mu_2, \max \mu_2)$.
end while
Output $D_l$ and $D_s$.
```

4.2. Optimization of image decomposition and completion model

By introducing the auxiliary variables $\boldsymbol{X}_l$ and $\boldsymbol{X}_s$, the objective function in Eq. (6) can be re-formulated as:

$$\begin{aligned} \left\{ \begin{array}{c} \boldsymbol{X}, \boldsymbol{X}_l, \boldsymbol{X}_s \\ \boldsymbol{A}_l, \boldsymbol{A}_s \end{array} \right\} = \arg \min_{\boldsymbol{X}, \boldsymbol{X}_l, \boldsymbol{X}_s, \boldsymbol{A}_l, \boldsymbol{A}_s} & \{ \|\boldsymbol{X} - \boldsymbol{X}_l - \boldsymbol{X}_s\|_F^2 + \tau \|\boldsymbol{X}\|_* \\ & + \beta_1 \|\boldsymbol{X}_l\|_* + \|\boldsymbol{X}_l - \boldsymbol{D}_l \boldsymbol{A}_l\|_F^2 \\ & + \beta_2 \|\boldsymbol{X}_s\|_1 + \|\boldsymbol{X}_s - \boldsymbol{D}_s \boldsymbol{A}_s\|_F^2 + \beta_3 \|\boldsymbol{A}_l\|_{2,1} + \beta_4 \|\boldsymbol{A}_s\|_1 \} \\ & s.t. \quad \boldsymbol{P}_\Omega(\boldsymbol{X}) = \boldsymbol{P}_\Omega(\boldsymbol{M}) \end{aligned} \tag{24}$$

4.2.1. Updating of X

We update $\boldsymbol{X}$ with other variables fixed, Eq. (24) can be simplified as:

$$\boldsymbol{X} = \arg \min_{\boldsymbol{X}} \{ \|\boldsymbol{X} - \boldsymbol{X}_l - \boldsymbol{X}_s\|_F^2 + \tau \|\boldsymbol{X}\|_* \} \quad s.t. \quad \boldsymbol{P}_\Omega(\boldsymbol{X}) = \boldsymbol{P}_\Omega(\boldsymbol{M}) \tag{25}$$

Eq. (25) can be solved by inexact Augmented Lagrangian multiplier method. The augmented Lagrangian function of Eq. (25) is:

$$\begin{aligned} \boldsymbol{X} = \arg \min_{\boldsymbol{X}} & \{ \|\boldsymbol{X} - \boldsymbol{X}_l - \boldsymbol{X}_s\|_F^2 + \tau \|\boldsymbol{X}\|_* + tr[\boldsymbol{\Lambda}^T (\boldsymbol{P}_\Omega(\boldsymbol{X}) - \boldsymbol{P}_\Omega(\boldsymbol{M}))] \\ & + \frac{\lambda}{2} \|\boldsymbol{P}_\Omega(\boldsymbol{X}) - \boldsymbol{P}_\Omega(\boldsymbol{M})\|_F^2 \} \end{aligned} \tag{26}$$

where $\boldsymbol{\Lambda}$ is the Lagrange multiplier, $\lambda (\lambda > 0)$ is the balance parameter.

To solve the above optimization problem, we introduce auxiliary variable $\widetilde{\boldsymbol{X}}$ and Eq. (26) can be rewritten as:

$$\begin{aligned} \{\boldsymbol{X}, \widetilde{\boldsymbol{X}}\} = \arg \min_{\boldsymbol{X}, \widetilde{\boldsymbol{X}}} & \{ \|\widetilde{\boldsymbol{X}} - \boldsymbol{X}_l - \boldsymbol{X}_s\|_F^2 + \tau \|\boldsymbol{X}\|_* \\ & + \frac{\lambda}{2} \|\boldsymbol{P}_\Omega(\widetilde{\boldsymbol{X}}) - \boldsymbol{P}_\Omega(\boldsymbol{M}) + \frac{\boldsymbol{\Lambda}}{\lambda}\|_F^2 + \|\boldsymbol{X} - \widetilde{\boldsymbol{X}}\|_F^2 \} \end{aligned} \tag{27}$$

$\widetilde{\boldsymbol{X}}$ can be updated by:

$$\widetilde{\boldsymbol{X}} = \arg \min_{\widetilde{\boldsymbol{X}}} \{ \|\widetilde{\boldsymbol{X}} - \boldsymbol{X}_l - \boldsymbol{X}_s\|_F^2 + \frac{\lambda}{2} \|\boldsymbol{P}_\Omega(\widetilde{\boldsymbol{X}}) - \boldsymbol{P}_\Omega(\boldsymbol{M}) + \frac{\boldsymbol{\Lambda}}{\lambda}\|_F^2 + \|\boldsymbol{X} - \widetilde{\boldsymbol{X}}\|_F^2 \} \tag{28}$$

which has closed-form solution:

$$\widetilde{\boldsymbol{X}} = 0.5(\widetilde{\boldsymbol{X}} + \boldsymbol{X}_l + \boldsymbol{X}_s) - 0.25\lambda P_\Omega(\widetilde{\boldsymbol{X}} - \boldsymbol{M}) - 0.25 P_\Omega(\boldsymbol{\Lambda}) \tag{29}$$

After $\widetilde{\boldsymbol{X}}$ is updated, we can obtain $\boldsymbol{X}$ by solving:

$$\boldsymbol{X} = \arg \min_{\boldsymbol{X}} \{ \|\boldsymbol{X} - \widetilde{\boldsymbol{X}}\|_F^2 + \tau \|\boldsymbol{X}\|_* \} \tag{30}$$

$\boldsymbol{X}$ can be solved by using the SVT algorithm.

4.2.2. Updating of $\mathbf{X}_l$ and $\mathbf{X}_s$

By fixing other parameters to update $\boldsymbol{X}_l$, Eq. (24) can be re-written as:

$$\boldsymbol{X}_l = \arg \min_{\boldsymbol{X}_l} \{ \|\widehat{\boldsymbol{X}_l} - \widehat{\boldsymbol{I}} \boldsymbol{X}_l\|_F^2 + \beta_1 \|\boldsymbol{X}_l\|_* \} \tag{31}$$

where $\widehat{\boldsymbol{X}_l} = [\boldsymbol{X} - \boldsymbol{X}_s; \boldsymbol{D}_l \boldsymbol{A}_l]$, $\widehat{\boldsymbol{I}} = [\boldsymbol{I}_W; \boldsymbol{I}_W]$, $\boldsymbol{I}_W$ represents $W \times W$ identity matrix. Eq. (31) is also a nuclear norm minimization problem which can be solved by SVT algorithm. Similarly, we can obtain $\boldsymbol{X}_s$ by solving:

$$\boldsymbol{X}_s = \arg \min_{\boldsymbol{X}_s} \{ \|\widehat{\boldsymbol{X}_s} - \widehat{\boldsymbol{I}} \boldsymbol{X}_s\|_F^2 + \beta_2 \|\boldsymbol{X}_s\|_1 \} \tag{32}$$

where $\widehat{\boldsymbol{X}_s} = [\boldsymbol{X} - \boldsymbol{X}_l; \boldsymbol{D}_s \boldsymbol{A}_s]$. Eq. (32) can be solved by TwIST or FIST algorithm.

4.2.3. Updating of $\mathbf{A}_l$ and $\mathbf{A}_s$

After $\boldsymbol{X}$, $\boldsymbol{X}_l$ and $\boldsymbol{X}_s$ are updated, $\boldsymbol{A}_l$ and $\boldsymbol{A}_s$ can be obtained by solving:

$$\boldsymbol{A}_l = \arg \min_{\boldsymbol{A}_l} \{ \|\boldsymbol{X}_l - \boldsymbol{D}_l \boldsymbol{A}_l\|_F^2 + \beta_3 \|\boldsymbol{A}_l\|_{2,1} \} \tag{33}$$

and

$$\boldsymbol{A}_s = \arg \min_{\boldsymbol{A}_s} \{ \|\boldsymbol{X}_s - \boldsymbol{D}_s \boldsymbol{A}_s\|_F^2 + \beta_4 \|\boldsymbol{A}_s\|_1 \} \tag{34}$$

Eq. (33) is a $l_{2,1}$-norm minimization problem which can be solved by the algorithm in literature [32]. Eq. (34) is l_1-norm minimization problem and $\boldsymbol{A}_s$ can be updated by TwIST or FIST algorithm. The details of solving the image decomposition and completion model are summarized in Algorithm 2.

Algorithm 2 Algorithm for the proposed image decomposition and completion model

```
Input: $M$, $D_l$, $D_s$, $\beta_j (j = 1, 2, \ldots, 4)$, $\tau$, maximum number of iterations $\mathcal{L}$.
Initialize: $X = M$, $\Lambda = 0$, $\lambda = 0$, $max\lambda = 10^{30}$, $\rho = 1.1$
while $\mathcal{L}$ not be reached do
  1. Update the underlying complete image $X$
      (1)Update auxiliary variable $\widetilde{X}$ by solving Eq. (29).
      (2)Update $X$ by solving Eq. (30).
  2. Update the low-rank and sparse components $X_l$ and $X_s$
      (1) Update $X_l$ by solving Eq. (31).
      (2) Update $X_s$ by solving Eq. (32).
  3. Update the coding coefficients $A_l$ and $A_s$
      (1) Update $A_l$ by solving Eq. (33).
      (2) Update $A_s$ by solving Eq. (34).
  4. Update $\Lambda$ and $\lambda$
      (1) $\Lambda = \Lambda + \lambda P_\Omega(X - M)$.
      (2) $\lambda = \min(\rho\lambda, max\lambda)$.
end while
Output $A_l$ and $A_s$.
```

Fig. 2. The performance analysis of the proposed image decomposition and completion model. .
(a) image with 20% missing pixels
(b) low-rank component obtained by the proposed image decomposition and completion model
(c) sparse component obtained by the proposed image decomposition and completion model
(d) superposition of low-rank and sparse component.

4.3. Convergence analysis

In the process of solving Eqs. (5) and (6), l_1-norm minimization, $l_{2,1}$-norm minimization and kernel norm minimization are mainly involved. Eqs. (10), (16), (32) and (34) are l_1-norm minimization problems, which can be solved by the TwIST or FIST algorithm. They have been proved to be convergent respectively [30,31]. Eqs. (15) and (33) are the $l_{2,1}$-norm minimization problem. The convergence of the optimization algorithm of this kind of problem has been proved in [32]. Moreover, Eqs. (19), (30), and (31) are nuclear norm minimization problems that can be solved by the SVT algorithm, the convergence of which has been proved in [22]. Therefore, we can conclude that both Algorithm 1 and Algorithm 2 are convergent.

4.4. Performance of the proposed image decomposition and completion model

In order to demonstrate the effectiveness of the proposed image decomposition and completion model, an experiment on the image with 20% missing pixels is carried out. The experimental results are shown in Fig. 2. Specifically, Fig. 2(a) shows an image with 20% missing pixels. Fig. 2(b) and (c) are the results of decomposition and completion of the damaged images, representing the low-rank component and sparse component respectively. Fig. 2(d) is the superposition of Fig. 2(b) and (c). Comparing Fig. 2(d) with (a), it can be seen that the proposed model can effectively recover the damaged images. The low-rank and sparse components as shown in Fig. 2(b) and (c) will be used for image fusion. In Section 6, extensive experiments will be carried out to verify the effectiveness and superiority of the proposed image fusion and completion framework.

5. Fusion scheme

In the related SR-based fusion methods, the activity level of an image patch can be measured by the l_1-norm of its corresponding sparse coding coefficients. Moreover, the coding coefficients with larger l_1-norm correspond to patches with salient features such as edge structures and texture details [11,12], the maximum l_1-norm fusion rule is thus chosen. Let L be the number of input images, each image is divided into P patches with the size of $\sqrt{W} \times \sqrt{W}$. $\boldsymbol{a}^j_{l,i}$ and $\boldsymbol{a}^j_{s,i}$ denote the coding coefficients of low-rank and sparse components of ith patch in the jth image respectively. The coding coefficients of final fused image can be obtained by:

$$\boldsymbol{a}^F_{c,i} = \boldsymbol{a}^{\hat{j}}_{c,i}, \hat{j} = \arg\max_{j} \left\{ \|\boldsymbol{a}^1_{c,i}\|_1, \|\boldsymbol{a}^2_{c,i}\|_1, \dots, \|\boldsymbol{a}^j_{c,i}\|_1, \dots, \|\boldsymbol{a}^L_{c,i}\|_1 \right\}, i = 1, 2, \dots, P, \tag{35}$$

where $c \in \{l, s\}$, $\boldsymbol{a}^F_{l,i}$ and $\boldsymbol{a}^F_{s,i}$ represent the fused coding coefficients of low-rank and sparse components of ith patch in jth image respectively. According to Eq. (35), we can obtain the fused low-rank and sparse coding coefficients, which can be expressed as $\boldsymbol{A}^F_l = [\boldsymbol{a}^F_{l,1}, \boldsymbol{a}^F_{l,2}, \dots, \boldsymbol{a}^F_{l,P}] \in \mathbb{R}^{K\times P}$ and $\boldsymbol{A}^F_s = [\boldsymbol{a}^F_{s,1}, \boldsymbol{a}^F_{s,2}, \dots, \boldsymbol{a}^F_{s,P}] \in \mathbb{R}^{K\times P}$. Then, the fused result can be obtained based on dictionaries $\boldsymbol{D}_l$ and $\boldsymbol{D}_s$:

$$\boldsymbol{X}^F = \boldsymbol{D}_l \boldsymbol{A}^F_l + \boldsymbol{D}_s \boldsymbol{A}^F_s \tag{36}$$

The final goal can be achieved by reshaping $\boldsymbol{X}^F$ to size of input image.

6. Experiment results

6.1. Experimental settings

Three pairs of images including one pair of medical images, one pair of infrared and visible images, and one pair of multi-focus images are selected for testing. The values of 10% or 20% pixels of each image are randomly set to zero to generate corresponding damaged images. The clean images without missing pixels and the damaged images with 10% and 20% missing pixels are presented in Fig. 3. The subfigures (a) to (f) are three pairs of clean images, while (g) to (l) are the damaged images with 10% missing pixels. The subfigures (m) to (r) are the damaged images with 20% missing pixels.

The proposed method is compared with the state-of-the-art methods including the ASR-based method [16], Kim's method [33], U2Fusion method [34], the KSVD-based method [14], Li's method [12] and Tao's method [29] for the clean image fusion. For the damaged image fusion, no method to deal with image fusion and completion simultaneously has been found in literature according to the authors' knowledge. Therefore, on the one hand, we regard the missing pixels as noise and compare the proposed method with those that can conduct simultaneous fusion and denoising, such as Li's method [12] and Tao's method [29]. On the other hand, the proposed method is compared with the step-by-step methods of image fusion and completion. During the step-by-step operation, to avoid the influence of missing pixels on the final result, image completion is carried out before image fusion. Image completion is performed by the Singular Value Thresholding (SVT) [22] and Truncated Nuclear Norm Regularization (TNNR) [35] algorithms, while U2Fusion [34] and KSVD-based [14] methods are used for image fusion. The four step-by-step methods are named SVT-U2Fusion, SVT-KSVD, TNNR-U2Fusion and TNNR-KSVD in the following.

For the purpose of evaluating the performance of each method quantitatively, Q_{NCIE} [36], Q_{MI} [37], Q_C [38], Q_{CB} [39], Q_{STD}, Q_{ENT} and $Q_{AB/F}$ [40] are adopt to measure the final experimental results. Q_{NCIE}, denoting the nonlinear correlation information entropy,

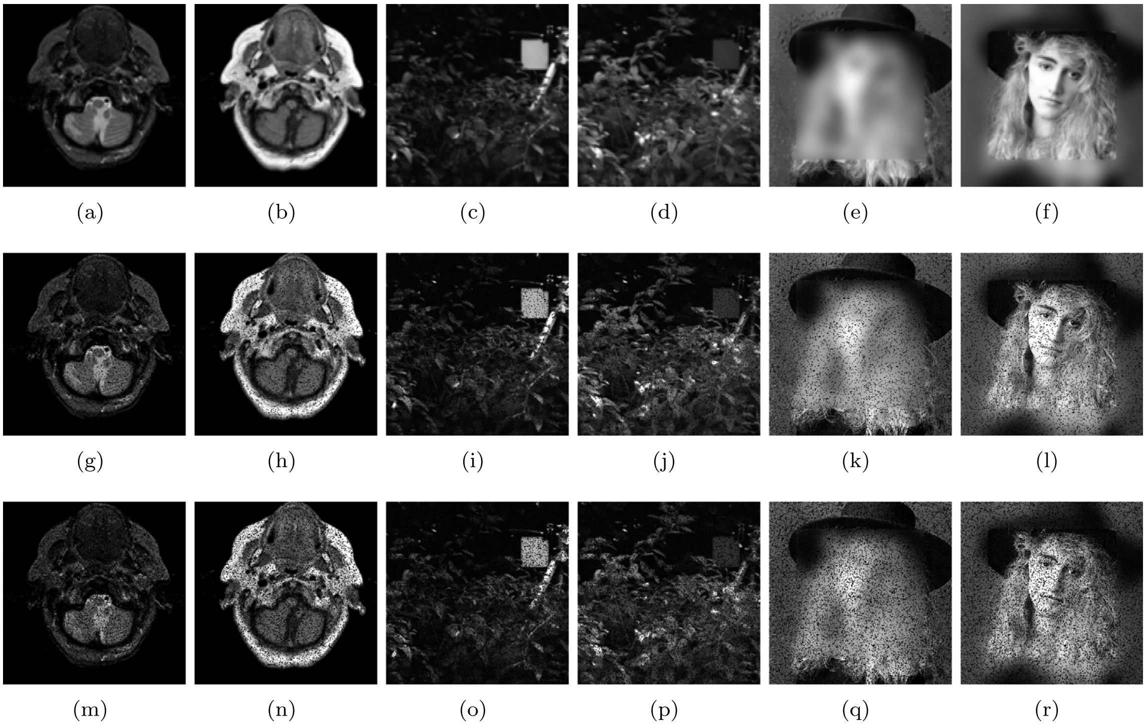

Fig. 3. The clean and damaged test images.
(a) to (f): three pairs of clean images without missing pixels
(g) to (l): three pairs of damaged images with 10% missing pixels
(m) to (r): three pairs of damaged images with 20% missing pixels.

is used to measure the correlation between the result image and source images. Mutual information Q_{MI} measures the information transferred from source images to the result image. Q_C represents the structural similarity between the result image and source images. Q_{CB} measures the similarity between the result image and source images based on human perception. Q_{STD} is the standard deviation of images. Q_{ENT} is the information entropy, which reflects the average information of images. $Q_{AB/F}$ is utilized to measure the amount of edge information transferred from the source images to the fused image. Larger value of the indicators implies better image quality.

6.2. Parameter settings

There are 11 parameters in dictionary learning and image decomposition algorithms. Each parameter is manually adjusted according to the empirical experience. Algorithm 1 includes five parameters: $\lambda_i (i = 1, 2, 3, 4)$ and the maximum number of iterations $\mathcal{K}$. In dictionary training, when the dictionaries generated by two adjacent iterations do not change much, that is, when $\|\boldsymbol{D}_l^{k+1} - \boldsymbol{D}_l^{k}\|_F^2$ and $\|\boldsymbol{D}_s^{k+1} - \boldsymbol{D}_s^{k}\|_F^2$ (k denoting the number of iterations) tend to zero, Algorithm 1 converges and the iteration ends. For the training samples given in Fig. 4, we obtain the convergence curves of Algorithm 1, as shown in Fig. 5.. When the number of iterations reaches 20, the change curves of low-rank and sparse dictionaries begin to converge. Therefore, we set $\mathcal{K} = 30$. In addition, we set $\lambda_1 = 0.001$, $\lambda_2 = 0.0001$, $\lambda_3 = 1.3$ and $\lambda_4 = 0.01$ in Algorithm 1. The detailed analysis of parameter $\lambda_i (i = 1, 2, 3, 4)$ is given in Section 6.5.

Algorithm 2 has six parameters, namely $\beta_j (j = 1, 2, 3, 4)$, τ and the maximum number of iterations $\mathcal{L}$. In the experiments, Algorithm 2 converges when the coding coefficients of low-rank and sparse components are stable. Fig. 6(a) and (b) show the convergence curves of Algorithm 2 on the clean image (in Fig. 3 (b)). Fig. 6(c) and (d) show the convergence curves of Algorithm 2 on the damaged image (in Fig. 3(h)). As shown in Fig. 6, Algorithm 2 converges when $\mathcal{L} = 15$, so we set $\mathcal{L} = 20$ for the clean and damaged image decomposition. The constraint term $\tau\|\boldsymbol{X}\|_*$ and condition term $\boldsymbol{P}_\Omega(\boldsymbol{X}) = \boldsymbol{P}_\Omega(\boldsymbol{M})$ in Eq. (6) are used to solve the problem of image completion. Therefore, when the clean images are fused, the condition term $\boldsymbol{P}_\Omega(\boldsymbol{X}) = \boldsymbol{P}_\Omega(\boldsymbol{M})$ is removed. τ is set to 0 and 0.1 for the clean and damaged image, respectively, as well as β_1, which is set to 20 and 0.1 for the clean and damaged image, respectively. For the clean and damaged image, $\beta_2 = 0.00001$, $\beta_3 = 0.1$, $\beta_4 = 0.00001$ in Algorithm 2. The detailed parameter analysis is shown in Section 6.5. Moreover, the dictionary size is set to 64×256 and the size of image block is 8×8 [12]. In order to reduce the blocking effect, six pixels are overlapped between adjacent image blocks.

6.3. Experiments on clean images without missing pixels

Three pairs of clean images without missing pixels are taken as test images to verify the effectiveness of the proposed method for clean image fusion, as shown in Fig. 3. Fig. 3(a) and (b) are a pair of MR-T1/MR-T2 medical images. MR-T1/MR-T2 images contain complementary information, which is used to produce a high-quality image for subsequent image processing. Fig. 3(c) and (d) are one pair of infrared–visible images. Fig. 3(c) is an infrared image that gives the characteristics of the thermal target but cannot reflect the details of the scene. Fig. 3(d) is a visible image that reflects the detailed information. Therefore, the infrared–visible image fusion can produce an image with clear background and thermal target. Fig. 3(e) and (f) are one pair of multi-focus images. The focus areas of the two images are different, and a clear image with the full focus can be obtained by image fusion.

Fig. 7 shows the fused results of clean images by the ASR-based, Kim's, U2Fusion, KSVD-based, Li's, Tao's and the proposed methods, respectively. Fig. 7(a) to (g) are the fused results of clean medical images. Fig. 7(h) to (n) lists the fused results of clean infrared–visible images, and Fig. 7(o) to (u) presents the fused results of clean multi-focus images. The local regions of the fused images are enlarged for further observation and comparison. As shown in Fig. 7(a) to (d),

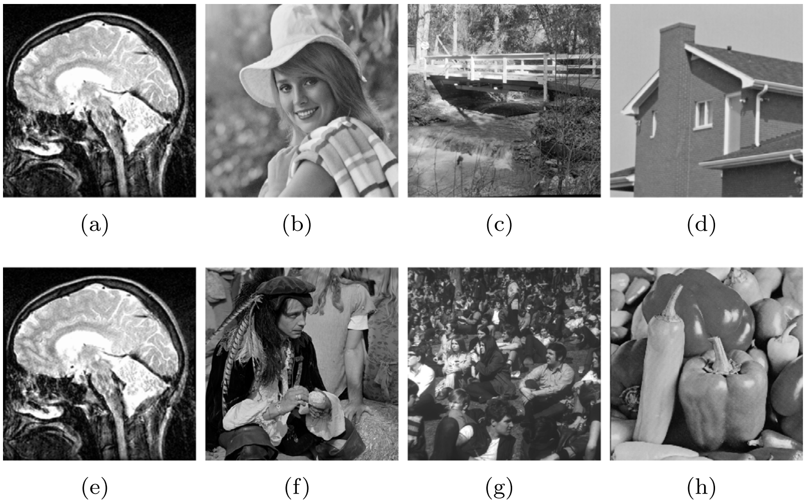

(a) (b) (c) (d)

(e) (f) (g) (h)

Fig. 4. The training samples for dictionary learning.

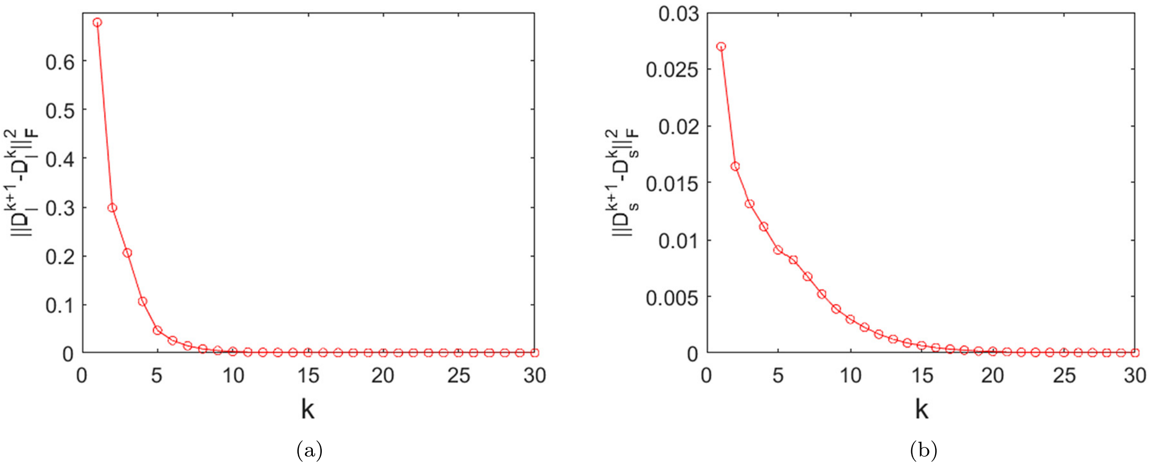

(a) (b)

Fig. 5. The convergence curves of low-rank and sparse dictionaries in Algorithm 1. .
(a) convergence curve of low-rank dictionaries $\boldsymbol{D}_l$; (b) convergence curve of low-rank dictionaries $\boldsymbol{D}_s$.

Fig. 7(h) to (k) and Fig. 7(o) to (r) are of low brightness, which means that the ASR, Kim's, U2Fusion and KSVD-based methods cannot retain the brightness information of the source images well. Moreover, the fused images shown in Fig. 7(a) to (d) and Fig. 7(p) to (r) present blurred details. Information loss can be told from the fused images shown in Fig. 7(h) to (k). As shown in Fig. 7(e) to (g), Fig. 7(l) to (n) and Fig. 7(s) to (u), the proposed method gives similar fusion results with Li's and Tao's methods. These fusion results present high brightness and clear details. It is because that the proposed method mainly deals with the fusion of damaged images whereas it lacks an obvious advantage in visual effect for the fusion of clean images.

We calculate Q_{NCIE}, Q_{MI}, Q_C, Q_{CB}, Q_{STD}, Q_{ENT} and $Q_{AB/F}$ for different fusion results to compare their performance quantitatively. Table 1 shows the quantitative assessments for clean image fusion results by different methods. As can be seen from Table 1, the proposed method outperforms the ASR-based, Kim's, U2Fusion, and KSVD-based methods in all metrics and is superior to Li's and Tao's methods at the most metrics. To summarize, for the clean image fusion, the proposed method outperforms others in terms of the visual and quantitative evaluation results. Then, we verify its performance in the damaged image fusion.

6.4. Experiments on images with missing pixels

Three pairs of damaged images with 10% missing pixels are selected as the test samples as shown in Fig. 3(g) to (l). Fig. 8 shows the comparison results obtained by SVT-U2Fusion, SVT-KSVD, TNNR-U2Fusion, TNNR-KSVD, Li's, Tao's and the proposed methods. Li's and Tao's methods cannot deal with the damaged image fusion, and the missing pixels are not compensated. Moreover, according to the recovery and fusion results of medical images in Fig. 8, SVT-U2Fusion and SVT-KSVD methods can retain the details of the original images, but with brightness loss. The results of TNNR-U2Fusion and TNNR-KSVD methods show poor visual effects with blurred details and low brightness. On the other hand, the results show that the proposed method retains the brightness and details in the original images, and the overall visual effect is the best among all tested methods. From the recovery and fusion results of infrared–visible images in Fig. 8, one can see that the proposed method achieves the best visual effect. However, the results of other methods suffer the loss of detailed information, particularly the results of TNNR-U2Fusion and TNNR-KSVD, which are seriously blurred. Furthermore, Fig. 8(o) to (u) show the experimental results of the multi-focus images. It can be seen from Fig. 8(o) to (r) that the missing pixels are not fully recovered by SVT-U2Fusion,

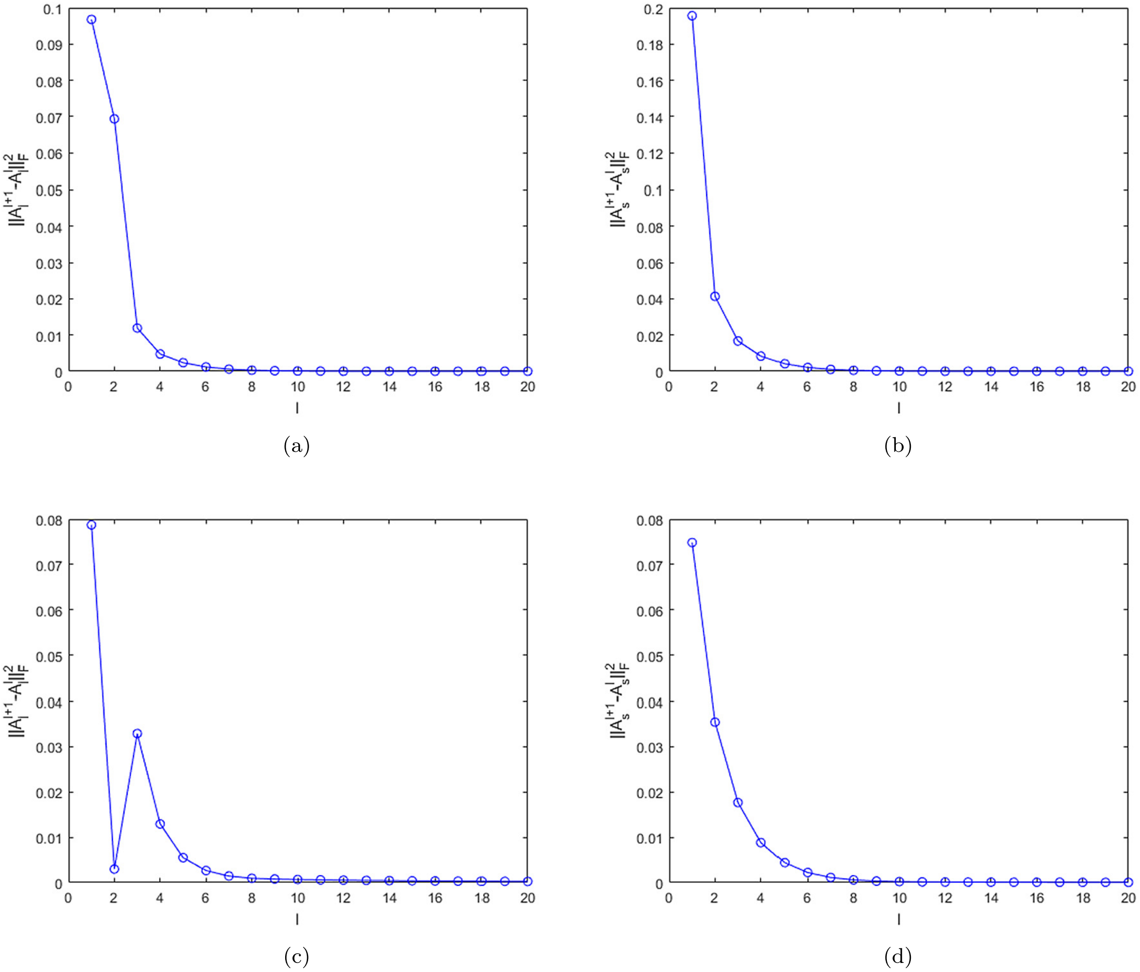

Fig. 6. The convergence curves of the low-rank and sparse coding coefficients in Algorithm 2.
(a) convergence curve of low-rank coding coefficients $\boldsymbol{A}_l$ on the clean image in Fig. 3(b)
(b) convergence curve of sparse coding coefficients $\boldsymbol{A}_s$ on the clean image in Fig. 3(b)
(c) convergence curve of low-rank coding coefficients $\boldsymbol{A}_l$ on the damaged image in Fig. 3(h)
(d) convergence curve of sparse coding coefficients $\boldsymbol{A}_s$ on the damaged image in Fig. 3(h).

Table 1
Quantitative evaluation of different fusion methods on the clean images without missing pixels.

Test images	Methods	Q_{NCIE}	Q_{MI}	Q_C	Q_{CB}	Q_{STD}	Q_{ENT}	$Q_{AB/F}$
MR-T1/MR-T2 (256 × 256)	ASR-based	0.8080	3.1831	0.6875	0.5736	51.2855	4.8278	0.5669
	Kim's	0.8079	3.1822	0.6745	0.5211	51.8338	5.2905	0.5006
	U2Fusion	0.8078	3.1756	0.3437	0.3503	41.7859	5.0637	0.3642
	KSVD-based	0.8083	3.2836	0.6903	0.5571	48.5748	5.0148	0.4956
	Li's	0.8129	4.2984	**0.8233**	0.5563	73.4829	**5.7402**	0.6503
	Tao's	0.8152	4.7027	0.7150	0.5857	73.8508	5.4249	0.6454
	Proposed	**0.8183**	**5.1911**	0.7353	**0.5972**	**75.3672**	5.4405	**0.6548**
Shrub (256 × 256)	ASR-based	0.8099	3.7771	0.7179	0.6464	35.0030	6.4952	0.6865
	Kim's	0.8098	3.7492	0.7747	0.6417	32.3807	6.5066	0.6603
	U2Fusion	0.8081	3.2782	0.6614	0.5893	29.9276	5.8206	0.5447
	KSVD-based	0.8101	3.8465	0.7034	0.6633	32.9276	6.4570	0.6412
	Li's	0.8147	4.7388	0.8122	0.6646	42.0075	**6.8485**	0.7183
	Tao's	0.8192	5.4041	0.8083	0.6857	**43.5986**	6.8242	**0.7253**
	Proposed	**0.8274**	**6.3169**	**0.8182**	**0.6939**	43.1467	6.7890	0.7242
Girl (256 × 256)	ASR-based	0.8153	**4.9663**	0.7918	0.6973	59.8548	7.6998	0.7722
	Kim's	0.8138	4.6227	0.8029	0.4935	58.3479	7.7134	0.6731
	U2Fusion	0.8138	4.5976	0.6538	0.6752	53.2722	7.3434	0.6059
	KSVD-based	0.8145	4.7829	0.7704	0.5665	58.7966	7.6636	0.7011
	Li's	0.8179	5.4972	0.8052	0.7396	61.9020	7.7375	0.7826
	Tao's	0.8139	4.6373	0.7945	0.6641	**65.6319**	**7.7553**	0.7522
	Proposed	**0.8231**	4.7649	**0.8050**	**0.7614**	63.1091	7.7550	**0.7829**

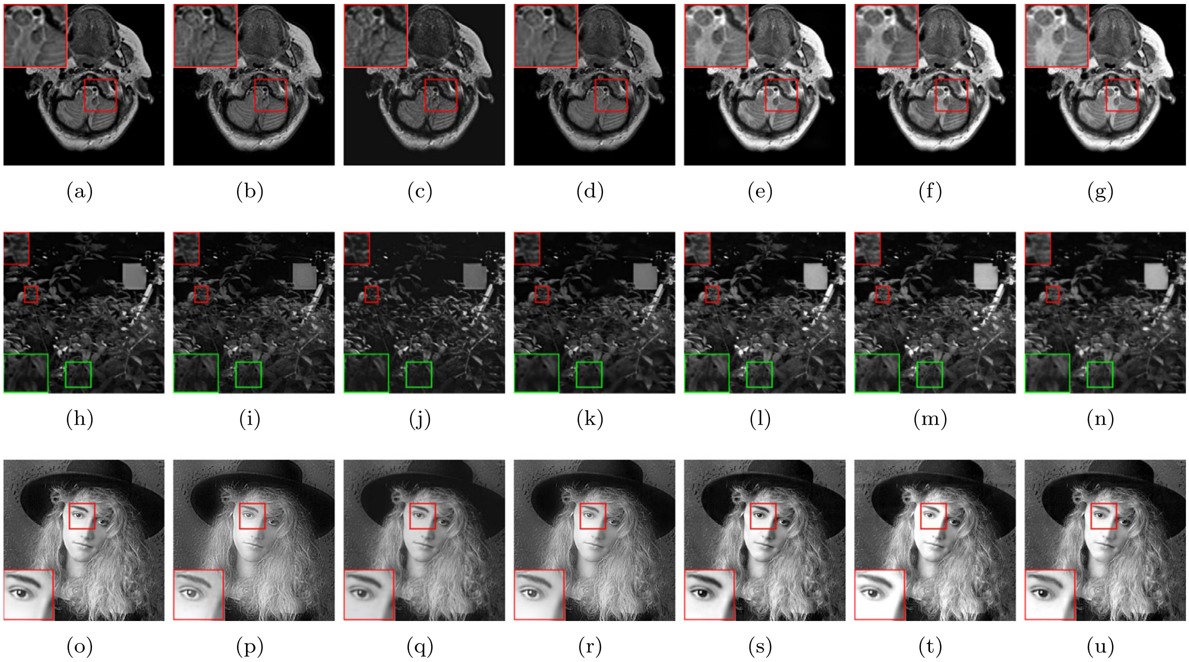

Fig. 7. The fused results of clean images.
(a) to (g): fused results of medical images by the ASR-based, Kim's, U2Fusion, KSVD-based, Li's, Tao's and the proposed methods
(h) to (n): fused results of infrared–visible images by the ASR-based, Kim's, U2Fusion, KSVD-based, Li's, Tao's and the proposed methods
(o) to (u): fused results of multi-focus images by the ASR-based, Kim's, U2Fusion, KSVD-based, Li's, Tao's and the proposed methods.

SVT-KSVD, TNNR-U2Fusion and TNNR-KSVD methods. The proposed method can well recover the lost pixels, and the resulting images achieve the optimal visual effect.

To further compare the performance of different methods, the recovery and fusion results are quantitatively analyzed. Table 2 presents the objective evaluation on the damaged images with 10% missing pixels. As shown in Table 2, for all the test images, the proposed method achieves the optimal results on most evaluation metrics, that is because the current evaluation metrics cannot always give objective evaluations for any image. Most evaluation metrics can give a consistent evaluation, which proves the superiority of this method.

The results obtained by the methods are compared on more challenging images with 20% missing pixels. Fig. 9 show the recovery and fusion results of medical images, infrared–visible images and multi-focus images obtained by different methods. From the visual point of view, the proposed method on those test images presents the best results among all tested methods. The quantitative comparison is shown in Table 3. From the visual and quantitative evaluation results, we can conclude that the developed method outperforms the compared methods in fusing the damaged images.

6.5. Parameter and constraint influence

In this section, Fig. 3(g) and (h) are used as test images to analyze the effects of parameter $\lambda_i (i = 1, 2, 3, 4)$ on the recovery and fusion results. For λ_i, it is found that when $\lambda_1 \in [0.00001, 0.005]$, the low-rank and sparse dictionaries obtained do not change much. With other parameters fixed, Fig. 10(a) to (c) illustrate the recovery and fusion results of Fig. 3(g) and (h) when $\lambda_1 = 0.000001, 0.001, 0.01$. As can be seen, compared with the result at $\lambda_1 = 0.001$, the results at $\lambda_1 = 0.000001, 0.01$ exist details blurred. So we set $\lambda_1 = 0.001$. When $\lambda_2 = 0.00001, 0.0001, 0.001$, the recovery and fusion results are shown in Fig. 10(d) to (f). When Fig. 10(d), (e) and (f) are compared, the details are the clearest at $\lambda_2 = 0.0001$. So we set $\lambda_2 = 0.0001$. When $\lambda_3 = 0.1, 1.3, 10$, the recovery and fusion results are shown in Fig. 10(g) to (i). It can be seen that $\lambda_3 = 1.3$ produces a more satisfactory result, so we set $\lambda_3 = 1.3$. When $\lambda_4 = 0.001, 0.01, 0.1$, the recovery and fusion results are shown in Fig. 10(j) to (l). As can be seen from Fig. 10(j) to (l), the result when $\lambda_4 = 0.01$ has the best visual effect. So we set $\lambda_4 = 0.01$. In summary, wet set λ_1, λ_2, λ_3 and λ_4 as 0.001, 0.0001, 1.3 and 0.01, respectively.

For the parameters in Eq. (6), Fig. 3(g) and (h) are used to analyze the influence of parameters on the fusion results of the damaged images, Fig. 3(a) and (b) are used to analyze the influence of parameters on the fusion results of the clean images.

In order to observe the effect of the parameter β_1, we set $\beta_1 = 0.1, 1, 10$ with $\beta_2 = 0.00001$, $\beta_3 = 0.1$, $\beta_4 = 0.00001$ and $\tau = 0.1$. Fig. 11(a) to (c) illustrate the recovery and fusion results of Fig. 3(g) and (h) under three different values of β_1. As can be seen from Fig. 11(a) to (c), when $\beta_1 = 0.1$, the visual effect of the final result is best and when $\beta_1 = 1, 10$, there are still pixels missing in the final results. Therefore, β_1 is set to 0.1. After a large number of experiments, we found that the recovery and fusion results of Fig. 3(g) and (h) have little difference in visual effect with $\beta_2, \beta_4 \in [0.000001, 0.001]$, so we set $\beta_2 = \beta_4 = 0.00001$. With other parameters fixed, Fig. 11(d) to (f) illustrate the recovery and fusion results of Fig. 3(g) and (h) when $\beta_3 = 0.1, 1, 10$. It can be seen that the results are blurred when $\beta_3 = 1, 10$, so we set $\beta_3 = 0.1$. For the parameter of τ, the final result does not change much when $\tau \in [0.01, 0.15]$. Fig. 11(g) to (i) demonstrate the recovery and fusion results of Fig. 3(g) and (h) under $\tau = 0.001, 0.1, 1$. When $\tau = 0.001$, there is still pixels missing in the final result. When $\tau = 1$, the details of the final result are blurred. Consequently, we set $\tau = 0.1$. The condition term $\boldsymbol{P}_{\Omega}(\boldsymbol{X}) = \boldsymbol{P}_{\Omega}(\boldsymbol{M})$ in Eq. (6) has a great influence on the recovery and fusion results. Fig. 11(j) shows the fusion results of Fig. 3(g) and (h) without $\boldsymbol{P}_{\Omega}(\boldsymbol{X}) = \boldsymbol{P}_{\Omega}(\boldsymbol{M})$. It can be seen that the result is seriously blurred.

The constraint term $\tau\|\boldsymbol{X}\|_*$ and condition term $\boldsymbol{P}_{\Omega}(\boldsymbol{X}) = \boldsymbol{P}_{\Omega}(\boldsymbol{M})$ in Eq. (6) are used to solve the problem of image completion. Therefore, τ is set to 0 and the condition term $\boldsymbol{P}_{\Omega}(\boldsymbol{X}) = \boldsymbol{P}_{\Omega}(\boldsymbol{M})$ is removed in Eq. (6) for the fusion of the clean images. Furthermore, with other parameters fixed, Fig. 11(k) to (l) illustrate the fusion results of Fig. 3(a) and (b) when $\beta_1 = 1, 20$. The fusion result has the brightness and detail loss

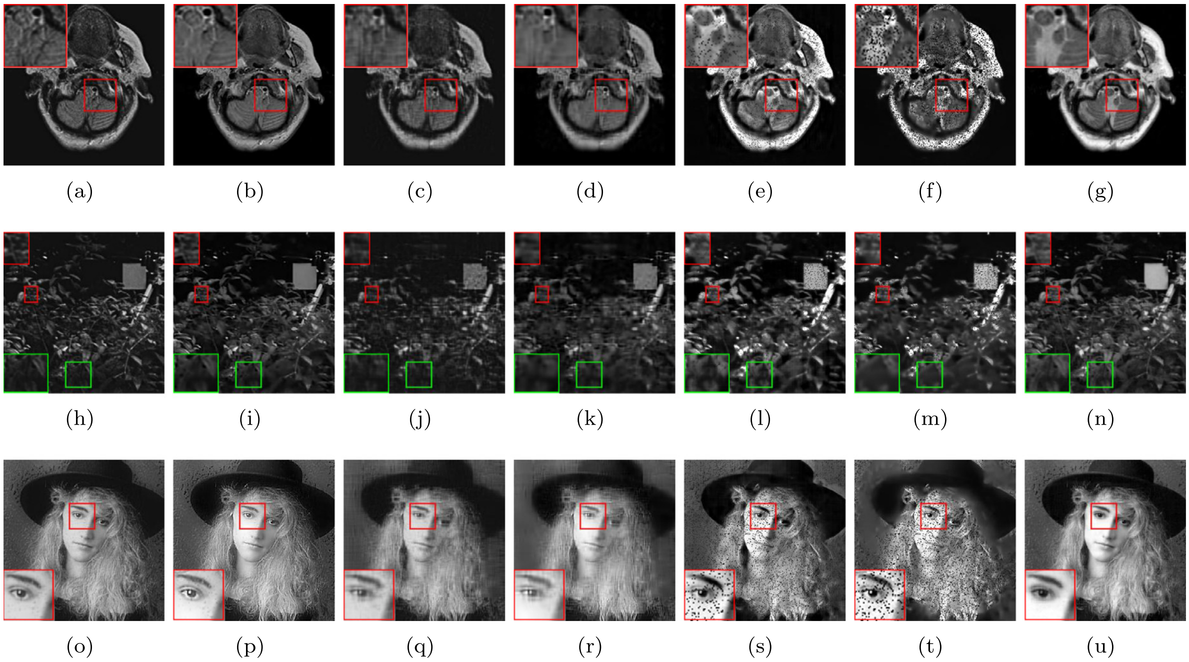

Fig. 8. The recovery and fusion results of the damaged images with 10% missing pixels.
(a) to (g): fused results of medical images by the SVT-U2Fusion, SVT-KSVD, TNNR-U2Fusion, TNNR-KSVD, Li's, Tao's and the proposed methods;
(h) to (n): fused results of infrared–visible images by the SVT-U2Fusion, SVT-KSVD, TNNR-U2Fusion, TNNR-KSVD, Li's, Tao's and the proposed methods;
(o) to (u): fused results of multi-focus images by the SVT-U2Fusion, SVT-KSVD, TNNR-U2Fusion, TNNR-KSVD, Li's, Tao's and the proposed methods.

Table 2
Quantitative evaluation of different fusion methods on the damaged images with 10% missing pixels.

Test images	Methods	Q_{NCIE}	Q_{MI}	Q_C	Q_{CB}	Q_{STD}	Q_{ENT}	$Q_{AB/F}$
MR-T1/MR-T2 (256 × 256)	SVT-U2Fusion	0.8038	3.1173	0.1768	0.2893	29.0939	5.1814	0.3572
	SVT-KSVD	0.8083	3.2799	0.6497	**0.5296**	48.3580	5.0755	0.4856
	TNNR-U2Fusion	0.8070	2.8655	0.3083	0.3384	40.6686	5.4114	0.2239
	TNNR-KSVD	0.8074	3.0055	0.4547	0.4553	46.9080	5.7684	0.2434
	Li's	0.8081	3.1923	0.3508	0.3897	**73.3170**	**6.3962**	0.3732
	Tao's	0.8076	3.0267	0.3106	0.3334	68.5787	5.9951	0.2466
	Proposed	**0.8100**	**3.7380**	**0.5249**	0.5221	69.7358	5.6447	**0.5539**
Shrub (256 × 256)	SVT-U2Fusion	0.8080	3.2506	0.6540	0.5853	29.6084	5.8125	0.5358
	SVT-KSVD	0.8100	3.8202	0.6991	0.6600	32.6302	6.4483	0.6260
	TNNR-U2Fusion	0.8059	2.4210	0.4504	0.5131	26.9033	5.8363	0.2587
	TNNR-KSVD	0.8065	2.7069	0.4682	0.5246	30.0391	6.5211	0.2619
	Li's	0.8067	2.7466	0.5668	0.5679	**48.0053**	6.3575	0.4127
	Tao's	0.8071	2.9091	0.4933	0.5187	42.7968	6.6115	0.3355
	Proposed	**0.8109**	**3.9436**	**0.7524**	**0.6577**	38.4243	**6.7030**	**0.6346**
Girl (256 × 256)	SVT-U2Fusion	0.8134	4.5056	0.6216	0.6450	52.9268	7.3441	0.5112
	SVT-KSVD	0.8140	4.6716	**0.7251**	0.5453	58.3607	7.6594	**0.5907**
	TNNR-U2Fusion	0.8122	4.2023	0.4201	0.5254	52.5511	7.3711	0.2075
	TNNR-KSVD	0.8130	4.4110	0.4370	0.4603	56.7154	7.6297	0.2231
	Li's	0.8111	3.8738	0.4202	0.5181	59.8385	7.6583	0.2865
	Tao's	0.8113	3.9512	0.3859	0.4534	42.7968	6.6115	0.2286
	Proposed	**0.8141**	**4.6830**	0.6925	**0.6960**	**60.1732**	**7.6651**	0.5281

at $\beta_1 = 1$, so we set $\beta_1 = 20$. Through the experiment, we found that the good fusion results can also be obtained for the clean images when $\beta_2 = 0.000001$, $\beta_3 = 0.1$, and $\beta_4 = 0.000001$. Generally, τ is set to 0 and 0.1 for the clean and damaged image, respectively, as well as β_1, which is set to 20 and 0.1 for the clean and damaged image, respectively. We set $\beta_2 = 0.00001$, $\beta_3 = 0.1$, $\beta_4 = 0.00001$ for the clean and damaged image.

6.6. Complexity analysis

The most complex parts of Algorithm 1 are to solve Eqs. (10), (15), (16) and (19), while the most complex parts of Algorithm 2 are to solve Eqs. (30)–(34). Specifically, Eqs. (10), (16), (32) and (34) are l_1-norm minimization problem, which can be solved by the TwIST algorithm. The TwIST algorithm costs $O(T_1T_2)$, where T_1 and T_2 denote the numbers of dual iterations. Eqs. (19), (30) and (31) are nuclear norm minimization problem, which can be solved by the SVT algorithm. The time consuming part of the SVT algorithm is $O(mn\min(m,n))$, where m and n are the number of row and column of input matrix [41]. Eqs. (15) and (33) are $l_{2,1}$-norm minimization problem, which can be solved by the algorithm proposed in [32]. The complexity of $l_{2,1}$ norm minimization algorithm is $O(T_{21})$, where T_{21} indicates the maximum number of iterations. In Algorithm 1, each of its iteration will cost $O(W^2K + T_1T_2 + T_{21})$, where W and K ($W < K$) are the dimensions of the input matrix D_l in Eq. (19). Therefore, the total complexity of Algorithm 1 is $O(\mathcal{K}(W^2K + T_1T_2 + T_{21}))$, where $\mathcal{K}$ is the number of iterations. In Algorithm 2, $\widetilde{\boldsymbol{X}} \in \mathbb{R}^{W\times P}$ and $\widehat{\boldsymbol{X}_l} \in \mathbb{R}^{2W\times P}$ are the input matrices of Eqs. (30) and (31), and updating both $\boldsymbol{X}$

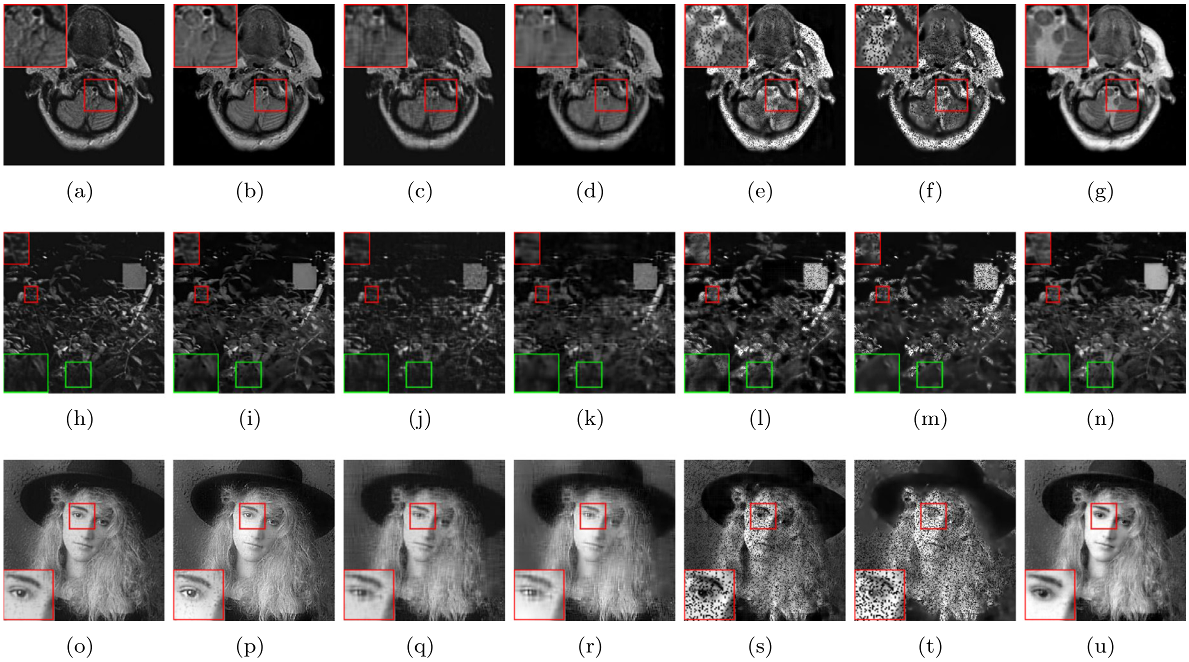

Fig. 9. The recovery and fusion results of the damaged images with 20% missing pixels.
(a) to (g): fused results of medical images by the SVT-U2Fusion, SVT-KSVD, TNNR-U2Fusion, TNNR-KSVD, Li's, Tao's and the proposed methods
(h) to (n): fused results of infrared–visible images by the SVT-U2Fusion, SVT-KSVD, TNNR-U2Fusion, TNNR-KSVD, Li's, Tao's and the proposed methods
(o) to (u): fused results of multi-focus images by the SVT-U2Fusion, SVT-KSVD, TNNR-U2Fusion, TNNR-KSVD, Li's, Tao's and the proposed methods.

Table 3
Quantitative evaluation of different fusion methods on the damaged images with 20% missing pixels.

Test images	Methods	Q_{NCIE}	Q_{MI}	Q_C	Q_{CB}	Q_{STD}	Q_{ENT}	$Q_{AB/F}$
MR-T1/MR-T2 (256 × 256)	SVT-U2Fusion	0.8076	3.0889	0.3589	0.3510	40.9322	5.1052	0.3391
	SVT-KSVD	0.8081	3.2400	**0.5595**	0.5085	47.9515	5.2311	0.4546
	TNNR-U2Fusion	0.8069	2.8597	0.3079	0.3410	40.6520	5.4112	0.2234
	TNNR-KSVD	0.8073	2.9965	0.4556	0.4547	46.9714	5.7739	0.2471
	Li's	0.8076	3.0464	0.3296	0.3804	**71.4005**	**6.3575**	0.2910
	Tao's	0.8076	3.0214	0.3091	0.3335	68.6809	5.9929	0.2462
	Proposed	**0.8097**	**3.6766**	0.5081	**0.5117**	69.3626	5.7144	**0.5270**
Shrub (256 × 256)	SVT-U2Fusion	0.8079	3.2104	0.6413	0.5867	28.9660	5.7949	0.5120
	SVT-KSVD	0.8098	3.7720	0.6924	**0.6535**	32.1299	6.4352	**0.5963**
	TNNR-U2Fusion	0.8059	2.4068	0.4485	0.5128	26.9212	5.8380	0.2547
	TNNR-KSVD	0.8065	2.6841	0.4676	0.5263	30.1288	6.5246	0.2622
	Li's	0.8059	2.4019	0.5193	0.5477	**45.8763**	**6.7794**	0.3516
	Tao's	0.8065	2.6818	0.4350	0.4955	41.9145	6.4452	0.2573
	Proposed	**0.8102**	**3.7894**	**0.7265**	0.6437	38.0150	6.7089	0.5961
Girl (256 × 256)	SVT-U2Fusion	0.8134	4.4249	0.6216	0.6450	52.9268	7.3441	0.4257
	SVT-KSVD	0.8135	4.5409	**0.6738**	0.5243	57.8551	7.6561	**0.4930**
	TNNR-U2Fusion	0.8120	4.1500	0.4178	0.5189	52.5867	7.3738	0.2036
	TNNR-KSVD	0.8127	4.3239	0.4341	0.4581	56.8488	7.6341	0.2191
	Li's	0.8094	3.3719	0.3713	0.4775	56.8527	7.5118	0.2124
	Tao's	0.8102	3.6246	0.3382	0.4194	**63.6426**	7.5732	0.1647
	Proposed	**0.8138**	**4.6098**	0.6535	**0.6472**	59.7336	**7.6685**	0.4536

and $\boldsymbol{X}_l$ will cost $O(W^2P)$. Thus, the total complexity of Algorithm 2 is $O(\mathcal{L}(W^2P+T_1T_2+T_{21}))$, where $\mathcal{L}$ is the maximum number of iterations.

7. Conclusion

In this paper, we proposed a joint implementation method of damaged image fusion and completion based on low-rank and sparse decomposition. The proposed method can perform image fusion and completion simultaneously to avoid the spread of artifacts that appears in the step-by-step operation. In the dictionary learning model, the constraints were imposed to improve the discriminability and accuracy of the low-rank and sparse dictionaries. Based on the learned dictionaries, an image decomposition and completion model was proposed, which can decompose an image into low-rank and sparse components, and recover the lost information of the image simultaneously. Moreover, the maximum l_1-norm fusion rule was used to fuse the coding coefficients of low-rank and sparse components, and the final recovery and fusion results were obtained. The proposed method was compared with the step-by-step operation of image fusion and completion. The experimental results showed that the proposed method outperforms the

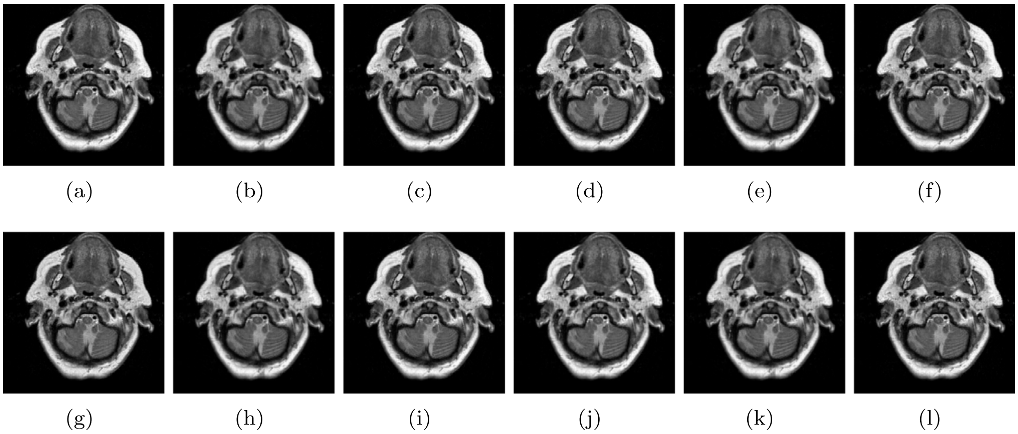

Fig. 10. The recovery and fusion results of Fig. 3(g) and (h) when the parameters λ_i are set to different values. .
(a) to (c): $\lambda_1 = 0.000001, 0.001, 0.01$ (d) to (f) $\lambda_2 = 0.00001, 0.0001, 0.001$ (g) to (i) $\lambda_3 = 0.1, 1.3, 10$ (j) to (l) $\lambda_4 = 0.001, 0.01, 0.1$.

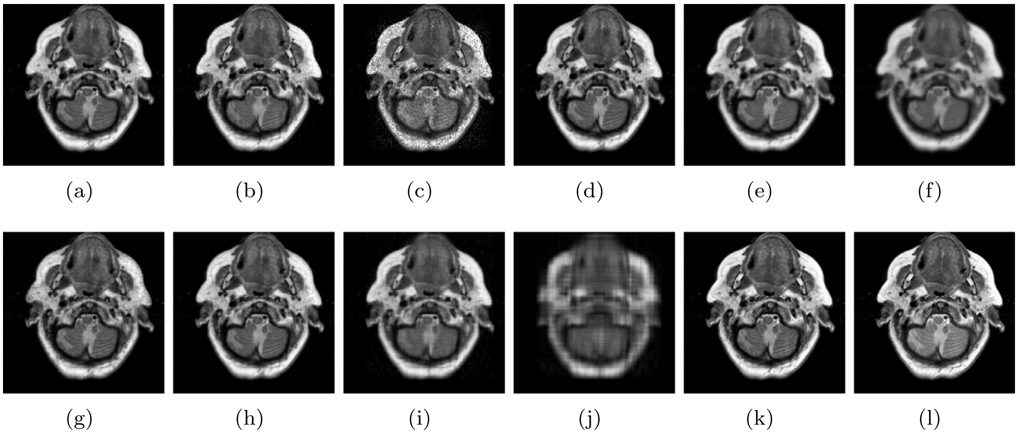

Fig. 11. Influence of the parameters and condition term on the fusion results in Eq. (6). .
(a) to (c): recovery and fusion results of Fig. 3(g) and (h) when $\beta_1 = 0.1, 1, 10$;
(d) to (f): recovery and fusion results of Fig. 3(g) and (h) when $\beta_3 = 0.1, 1, 10$;
(g) to (i): recovery and fusion results of Fig. 3(g) and (h) when $\tau = 0.001, 0.1, 1$;
(j): recovery and fusion results of Fig. 3(g) and (h) without the condition term $\boldsymbol{P}_{\Omega}(\boldsymbol{X}) = \boldsymbol{P}_{\Omega}(\boldsymbol{M})$;
(k) to (l): fusion results of the clean images in Fig. 3(a) and (b) when $\beta_1 = 1, 20$.

tested state-of-the-art methods in terms of both the visual effect and quantitative performance evaluation.

CRediT authorship contribution statement

Minghong Xie: Conceptualization, Methodology, Writing – original draft, Resources. **Jiaxin Wang:** Investigation, Data curation, Software, Validation. **Yafei Zhang:** Visualization, Supervision, Writing – reviewing & editing, Funding acquisition.

Declaration of competing interest

The authors declare that they have no known competing financial interests or personal relationships that could have appeared to influence the work reported in this paper.

Acknowledgments

This work was partly supported by the National Natural Science Foundation of China under Grant (61762056, 61562053, 61563025, 61763020, 61302041), and Yunnan Natural Science Funds, China under Grant (2017FB094).

References

[1] S. Li, X. Kang, L. Fang, J. Hu, H. Yin, Pixel-level image fusion: A survey of the state of the art, Inf. Fusion 33 (2017) 100–112.
[2] B. Meher, S. Agrawal, R. Panda, A. Abraham, A survey on region based image fusion methods, Inf. Fusion 48 (2019) 119–132.
[3] H. Li, X. Li, Z. Yu, C. Mao, Multifocus image fusion by combining with mixed-order structure tensors and multiscale neighborhood, Inform. Sci. 349–350 (2016) 25–49.
[4] S. Li, B. Yang, Multifocus image fusion using region segmentation and spatial frequency, Image Vis. Comput. 26 (7) (2008) 971–979.
[5] H. Li, B.S. Manjunath, S.K. Mitra, Multisensor image fusion using the wavelet transform, Graph. Models Image Process. 57 (3) (1995) 235–245.
[6] G. Pajares, J.M. de la Cruz, A wavelet-based image fusion tutorial, Pattern Recognit. 37 (9) (2004) 1855–1872.
[7] F. Nencini, A. Garzelli, S. Baronti, L. Alparone, Remote sensing image fusion using the curvelet transform, Inf. Fusion 8 (2) (2007) 143–156.
[8] H. Li, H. Qiu, Z. Yu, Y. Zhang, Infrared and visible image fusion scheme based on NSCT and low-level visual features, Infrared Phys. Technol. 76 (2016) 174–184.
[9] X. Li, H. Li, Z. Yu, Y. Kong, Multifocus image fusion scheme based on the multiscale curvature in nonsubsampled contourlet transform domain, Opt. Eng. 54 (7) (2015) 073115.
[10] Q. Zhang, B. long Guo, Multifocus image fusion using the nonsubsampled contourlet transform, Signal Process. 89 (7) (2009) 1334–1346.
[11] B. Yang, S. Li, Multifocus image fusion and restoration with sparse representation, IEEE Trans. Instrum. Meas. 59 (4) (2010) 884–892.
[12] H. Li, X. He, D. Tao, Y. Tang, R. Wang, Joint medical image fusion, denoising and enhancement via discriminative low-rank sparse dictionaries learning, Pattern Recognit. 79 (2018) 130–146.

[13] S. Li, H. Yin, L. Fang, Group-sparse representation with dictionary learning for medical image denoising and fusion, IEEE Trans. Biomed. Eng. 59 (12) (2012) 3450–3459.

[14] Z. Zhu, Y. Chai, H. Yin, Y. Li, Z. Liu, A novel dictionary learning approach for multi-modality medical image fusion, Neurocomputing 214 (2016) 471–482.

[15] Z. Zhu, H. Yin, Y. Chai, Y. Li, G. Qi, A novel multi-modality image fusion method based on image decomposition and sparse representation, Inform. Sci. 432 (2018) 516–529.

[16] Y. Liu, Z. Wang, Simultaneous image fusion and denoising with adaptive sparse representation, IET Image Process. 9 (5) (2015) 347–357.

[17] N. Yu, T. Qiu, F. Bi, A. Wang, Image features extraction and fusion based on joint sparse representation, IEEE J. Sel. Top. Sign. Proces. 5 (5) (2011) 1074–1082.

[18] X. Ma, S. Hu, S. Liu, J. Fang, S. Xu, Multi-focus image fusion based on joint sparse representation and optimum theory, Signal Process., Image Commun. 78 (2019) 125–134.

[19] Q. Hu, S. Hu, F. Zhang, Multi-modality medical image fusion based on separable dictionary learning and gabor filtering, Signal Process., Image Commun. 83 (2020) 115758.

[20] M. Elad, J.L. Starck, P. Querre, D.L. Donoho, Simultaneous cartoon and texture image inpainting using morphological component analysis (MCA), Appl. Comput. Harmon. Anal. 19 (2005) 340–358.

[21] E.J. Candès, B. Recht, Exact matrix completion via convex optimization, Found. Comput. Math. 9 (2009) 717.

[22] J.-F. Cai, E.J. Candès, Z. Shen, A singular value thresholding algorithm for matrix completion, SIAM J. Optim. 20 (4) (2008) 1956–1982.

[23] K.-C. Toh, S. Yun, An accelerated proximal gradient algorithm for nuclear norm regularized linear least squares problems, Pac. J. Optim. 6 (3) (2010) 615–640.

[24] Z. Lin, M. Chen, Y. Ma, The augmented lagrange multiplier method for exact recovery of corrupted low-rank matrices, Math. Program. 9 (2010).

[25] D. Zhang, Y. Hu, J. Ye, X. Li, X. He, Matrix completion by truncated nuclear norm regularization, in: 2012 IEEE Conference on Computer Vision and Pattern Recognition, Providence, 2012, pp. 2192–2199.

[26] Y. Jiang, M. Wang, Image fusion with morphological component analysis, Inf. Fusion 18 (2014) 107–118.

[27] Z. Liu, Y. Chai, H. Yin, J. Zhou, Z. Zhu, A novel multi-focus image fusion approach based on image decomposition, Inf. Fusion 35 (2017) 102–116.

[28] Y. Zhang, M. Yang, N. Li, Z. Yu, Analysis-synthesis dictionary pair learning and patch saliency measure for image fusion, Signal Process. 167 (2020) 107327.

[29] H. Li, Y. Wang, Z. Yang, R. Wang, X. Li, D. Tao, Discriminative dictionary learning-based multiple component decomposition for detail-preserving noisy image fusion, IEEE Trans. Instrum. Meas. 69 (4) (2020) 1082–1102.

[30] J.M. Bioucas-Dias, M.A.T. Figueiredo, A new twist: two-step iterative shrinkage/thresholding algorithms for image restoration, IEEE Trans. Image Process. 16 (12) (2007) 2992–3004.

[31] A. Beck, M. Teboulle, A fast iterative shrinkage-thresholding algorithm for linear inverse problems, SIAM J. Imaging Sci. 2 (1) (2009) 183–202.

[32] F. Nie, H. Huang, X. Cai, C.H.Q. Ding, Efficient and robust feature selection via joint L2, 1-norms minimization, in: International Conference on Nerual Information Processing Systems, 2010, pp. 1813–1821.

[33] M. Kim, D.K. Han, H. Ko, Joint patch clustering-based dictionary learning for multimodal image fusion, Inf. Fusion 27 (2016) 198–214.

[34] H. Xu, J. Ma, J. Jiang, X. Guo, H. Ling, U2fusion: A unified unsupervised image fusion network, IEEE Trans. Pattern Anal. Mach. Intell. (2020) 1.

[35] Y. Hu, D. Zhang, J. Ye, X. Li, X. He, Fast and accurate matrix completion via truncated nuclear norm regularization, IEEE Trans. Pattern Anal. Mach. Intell. 35 (9) (2013) 2117–2130.

[36] Q. Wang, Y. Shen, J. Jin, Performance evaluation of image fusion techniques, Image Fusion (2008) 469–492.

[37] G. Qu, D. Zhang, P. Yan, Information measure for performance of image fusion, Electron. Lett. 38 (7) (2002) 313–315.

[38] N. Cvejic, D.R. Bull, C.N. Canagarajah, Metric for multimodal image sensor fusion, Electron. Lett. 43 (2) (2007) 95–96.

[39] Y. Chen, R.S. Blum, A new automated quality assessment algorithm for image fusion, Image Vis. Comput. 27 (10) (2009) 1421–1432.

[40] V. Petrovi, C. Xydeas, On the effects of sensor noise in pixel-level image fusion performance, in: Proceedings of the Third International Conference on Information Fusion, Vol. 2, 2000, pp. WEC3/14–WEC3/19.

[41] T.-H. Oh, Y. Matsushita, Y.-W. Tai, I.S. Kweon, Fast randomized singular value thresholding for low-rank optimization, IEEE Trans. Pattern Anal. Mach. Intell. 40 (2) (2018) 376–391.